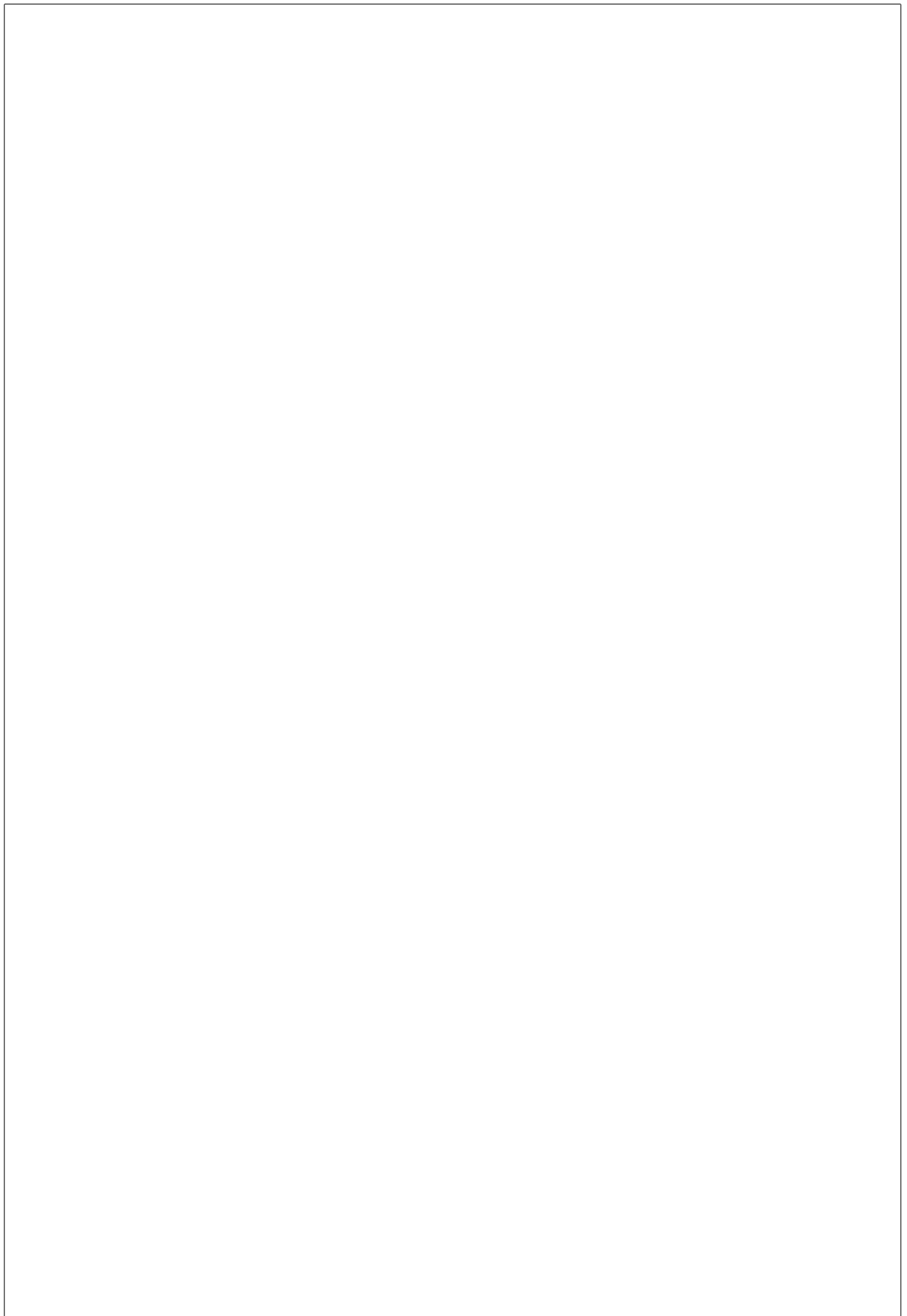


---

---



---

---

---

# Todo list

enter diVincenzo criteria . . . . .	1
saturation already introduced? . . . . .	4
thickness . . . . .	5
value . . . . .	5
value . . . . .	5
short discussion if resolution is enough . . . . .	5
check number . . . . .	6
insert chapter . . . . .	6
specs . . . . .	6
resolution CCD . . . . .	6
optical diffraction, shadows . . . . .	6
type . . . . .	6
fox nachlesen . . . . .	7
wording . . . . .	8
put in reference . . . . .	8
sind die nicht auch zermahlen worden? . . . . .	10
wie kommen da die SiVs rein? . . . . .	10
ueberleitung zu naechstem satz . . . . .	10
is this correct? . . . . .	11
irgendwo einfuegen, was ich diesbezgl. gemacht hab . . . . .	11
put in figure . . . . .	11
info about vibrational mill . . . . .	13
more info . . . . .	13
besser formulieren . . . . .	13
etwas anders fomulieren . . . . .	13
implantation parameters . . . . .	13
how much? . . . . .	15
time? . . . . .	15
check numbers . . . . .	17
sample name . . . . .	17
another citation . . . . .	19
warum . . . . .	19
type . . . . .	20
check number . . . . .	20
input Adam Gali . . . . .	26

---

---

---

**Extra long title which spans several lines and therefore  
has to be split manually and the vertical spacing  
has to be adjusted**

**My Name**

**My university**

**(Diploma/doctoral...) Thesis**

**Supervisor:**

**Prof. Dr. Supervisor**  
**Supervisor's Department, University of ...**

**March 2013**

---

---

**Abstract**

A novel method... It is based on...

---

---

---

# Contents

<b>Table of Contents</b>	i
<b>List of Figures</b>	ii
<b>List of Tables</b>	v
<b>Acknowledgements</b>	vi
<b>1 Introduction</b>	1
<b>2 The Awesome Theory</b>	3
<b>3 Photoluminescence Setup</b>	4
3.1 Confocal Setup . . . . .	4
3.2 Optical Imaging . . . . .	6
3.3 Spectrometer . . . . .	6
3.4 HBT . . . . .	7
<b>4 Fabrication of Nanodiamonds</b>	9
4.1 HPHT . . . . .	9
4.2 CVD . . . . .	10
4.3 Wet-Milling . . . . .	11
4.3.1 Wet-Milled HPHT Nanodiamonds . . . . .	13
4.3.2 Wet-Milled chemical vapor deposition Nanodiamonds . . . . .	13
4.3.3 Doubly Wet-Milled Implanted Nanodiamonds Implanted With Silicon .	15
4.4 Iridium Substrate . . . . .	17
4.4.1 Preparation of The Substrate . . . . .	18
<b>5 Crystal Quality of Nanodiamonds</b>	19
5.1 Annealing and Oxidation . . . . .	19
5.2 Raman Measurements . . . . .	19
5.3 TEM . . . . .	21
<b>6 Spectral Distribution</b>	22
6.0.1 Photoluminescence spectra . . . . .	22
6.1 g <sub>2</sub> Measurements . . . . .	28
6.1.1 Photostability . . . . .	30

<b>7 discussion</b>	<b>32</b>
<b>8 Conclusion</b>	<b>33</b>
<b>A Text of Minor Interest</b>	<b>34</b>
<b>Bibliography</b>	<b>35</b>
<b>Index</b>	<b>38</b>

---

---

# List of Figures

3.1	Confocal setup . . . . .	5
3.2	HBT, spectrometer . . . . .	5
4.1	SEM images of CVD grown diamonds (sample insitucvd) produced by M. Schreck's group (Augsburg University). The average size of these nanodiamonds is 100 nm. (a) Overview image, white dots are nanodiamonds. (b) Detail image, it can be seen that not all nanodiamonds exhibit the same size and that they coexist in different shapes. . . . .	10
4.2	Sketch showing the production of CVD nanodiamonds in the growth chamber with a methane gas environment. . . . .	10
4.3	Pictures of the milled nanodiamonds (sample insitu100). (a) SEM picture showing the distribution of the nanodiamond crystals on the iridium substrate. (b) TEM picture of a nanodiamond particle. . . . .	12
4.4	Sketch showing the wet-milling process in a vibrational mill. Vibrations from the mill drive the beads which collide with the diamond material and crush it to smaller pieces. . . . .	12
4.5	(a) SEM picture of nanodiamonds sunken into a silicon substrate after annealing at 900 °C for 3 h. Magnification 20 000. (b) SEM image of the microdiamonds after milling on an iridium substrate, but before implantation. In the middle of the picture, there is a reference cross milled into the iridium substrate with a focused ion beam. Its size amounts to 10 µm. It can be seen, that the microdiamonds exhibit sizes of a few micrometer. . . . .	14
4.6	(a) Microscope image of a drop of water on an iridium substrate cleaned with Piranha etch. This picture was used to estimate the contact angle. (b) SEM picture of an 60 nm iridium layer that peeled off the substrate after an ultrasonic bath. . . . .	17
5.1	Raman measurements, black: data, red: fit. (a) Raman measurement before oxidation, sample insitu70. The diamond Raman peak is situated at 1338 cm <sup>-1</sup> . The broad feature around 1600 cm <sup>-1</sup> corresponds to the graphite G-band. (b) Raman measurement after oxidation, sample insitu70o. The G-band has vanished, indicating removal of graphite and amorphous sp <sup>2</sup> hybridized carbon. . .	20

6.1	Distribution of the linewidth vs. the center wavelength of the ZPL of the investigated SiV centers in milled nanodiamonds containing <i>in-situ</i> incorporated SiV centers (samples insitu50, insitu70, insitu70n, insitu70o, insitu100). The data can be coarsely separated into two groups, H and V. The cross marks the position of an ideal SiV center in unstrained bulk diamond [23]. The red triangles indicate emitters which exhibited an antibunching dip in the $g^{(2)}(0)$ measurement. Upwards pointing triangles represent emitters which exhibit fluorescence intermittency (blinking), while triangles pointing down represent emitters which do not exhibit any blinking (see subsection 6.1.1). The inset displays a zoom into group V, a least squares linear regression to the data, and the 95% confidence interval of the regression as a shaded area around the fit line. A clear trend of broader linewidths for longer ZPL center shifts is visible.	23
6.2	PL spectra measured with sample insitu100ao. (a) A representative room temperature spectrum of one of the emitters in group H of Figure 6.1, denoted emitter emitter H1. (b) A representative room temperature spectrum of one of the emitters in group V of Figure 6.1, denoted emitter V1. The red lines are Lorentzian fits to the peaks. . . . .	24
6.3	Comparison of the distribution of the linewidth vs. the center wavelength of the ZPL of the investigated SiV centers in milled nanodiamonds with data measured on the same nanodiamonds reported by J. Benedikter in [24], with data measured on CVD nanodiamonds, with data measured in CVD diamonds by E. Neu in a filter window between 730 nm and 750 nm [25], and with data measured on implanted250ao, implanted with Silicon. Black symbols represent emitters exhibiting a dip in the $g^{(2)}(0)$ function, indicating a single or very few SiV centers . . . . .	24
6.4	Calculations of the wavelength of the SiV center ZPL in dependence of pressure. Black: hydrostatic pressure; other colors: uniaxial pressure, for different orientations and calculated with different functionals PBE and HSE. Hydrostatic-type pressure causes a moderate blue shift whereas uniaxial strain causes larger redshift with different magnitudes depending on the direction of the strain better description from Adam Gali . . . . .	25
6.5	Shift of dominant sideband peak from the ZPL in spectra of SiV centers (group V, samples insitu50, insitu70, insitu100) vs. ZPL center wavelength. The linear fit shows that the shift decreases with increasing ZPL center wavelength. The shaded area is the 95% confidence interval. . . . .	27
6.6	Representative spectrum of an emitter of group V exhibiting a sideband peak. . . . .	27
6.7	(a) Intensity autocorrelation function of emitter H1 at an excitation power of 15 $\mu$ W. (b) Intensity autocorrelation function of emitter V1 at an excitation power of 200 $\mu$ W, which is 25% of the saturation count rate. . . . .	28
6.8	Distribution of countrate of a blinking level vs. its retention time in this level. (a) Time trace of the single emitter exhibiting the highest blinking rate. The variation of the countrate in the upper state is attributed to a drift of the setup. (b) Detail of the time trace of the same emitter. . . . .	29

- 6.9 Retention times of the single emitter exhibiting the highest blinking rate in the bright (red) and dark (blue) states. The dashed line represents a kernel density estimation of the distribution of retention times. The y-axis is scaled to the normalized kernel density estimate. The red solid line is an exponential fit of the bright state retention times, the blue solid line is a lognormal fit of the dark state retention times. The fits are in good agreement with the data (p-values: red 0.92, blue 0.77) . . . . . 30

---

---

## List of Tables

4.1	Summary of the samples grown on diamondoid seed crystals. . . . .	12
4.2	Summary of the wet-milled samples. The first column indicates the names of the samples, the second the mean diameter of the nanodiamonds, and the third describes how the silicon was incorporated into the diamond. . . . .	16

---

---

# Acknowledgements

First of all, I want to thank my supervisor...

I am very grateful for the guiding help of...

I am grateful to...

---

---

# Chapter 1

## Introduction

“Every competent physicist can ‘do’ quantum mechanics, but the stories we tell ourselves about what we are doing are as various as the tales of Sheherazade, and almost as implausible.” - David J. Griffiths

Quantum optics is the sciences of light which deals with single light particles, namely photons. Within the last few years the topic of quantum technologies has witnessed a large progress in fields like quantum cryptography, quantum computation and quantum metrology. Requirements for these technologies are ideally single photons which are produced “on demand” i.e. deterministically and have well defined properties. For instance, quantum computing places restraints on the photon sources, called the diVincenzo criteria (). The progress of these technologies calls for measurement standards to make the individual measurements comparable???. The candela is the SI (système internationale) unit for optical radiation [1] and is the only unit which is linked to physiological processes, namely the varying sensitivity of the human eye to radiation of different frequencies. It is a photometric quantity, meaning that a physical measurement of the light in terms of luminous intensity represents the visual sensation experienced by a human observer exposed to the same source of light. It is one of the base units since the system was first introduced. In the latest definition, the candela is linked to the unit watt. The current definition of the candela (cd) is the following: “The candela is the luminous intensity, in a given direction, of a source that emits monochromatic radiation of frequency  $540 \times 10^{12}$  hertz and that has a radiant intensity in that direction of  $1/683$  watt per steradian.”[2] Advances in the quantum technologies which operate in the photon-counting regime would profit from a redefinition of the candela in terms of photon number, named “quantum candela”.

The term “quantum candela” is used to describe a reformulation of the candela by defining it via a countable number of photons. This new definition would be of a form that converts the current definition into

$$P = nh\nu \quad (1.1)$$

where

enter di-Vincenzo criteria

$P$  = power =  $1/683$  W exactly

$n$  = number of photons per second

$h$  = Planck's constant =  $6.626\,069\,3(11) \times 10^{-34}$  J s

$\nu$  = photon frequency =  $540 \times 10^{12}$  Hz exactly

which yields [1]

$$n = 4.091\,942\,9(70) \times 10^{15} \text{ s}^{-1}$$

The number of photons of all wavelengths emitted or contained in a given beam of light is given by [3]:

$$N_P = \int \frac{E_\nu}{h\nu} d\nu = \int \frac{\lambda E_\lambda}{hc} d\lambda \quad (1.2)$$

From this equation, the minimal number of photons to illuminate a scene can be calculated. However, in nature most light sources emit continuous light, therefore not the absolute number of photons, but the number of photons emitted per unit time, i.e. the photon flux  $\Phi_P$  is of interest:

$$\Phi_P = \frac{dN_P}{dt} \quad (1.3)$$

For high-accuracy absolute radiometry at the quantum level, predictable or quasi-single-photon sources and photon detectors are needed. A key requirement for the progress of quantum information technology is the development of sources that deterministically produce single photons upon request (on-demand source). Colour centres in synthetic diamond...represent an interesting single-photon source with strong anti-bunching and a spectral width about 1nm at room temperature. [3]

---

---

## Chapter 2

# The Awesome Theory

The Large Hadron Collider (LHC) is a particle collider which is situated near Geneva, Switzerland and lies about 100 m below ground level.

## Chapter 3

# Photoluminescence Setup

The key measurements of this thesis are spectroscopic measurements of SiV centers in nanodiamonds. For this aim, a home-built confocal setup is used, which is described in this chapter.

The confocal setup serves to perform a series of spectroscopic measurements on fluorescence light: scanning the sample to find SiV centers, recording photoluminescence spectra of the aforementioned, determining the brightness of an emitter by recording the saturation count rate, and determine whether the emitter in question is a single emitter by performing photon autocorrelation ( $g^{(2)}$ ) measurements. The entire setup is built up by a confocal setup, to which a spectrometer or an Hanbury Brown and Twiss setup are attached:

- The confocal setup is the core component where the sample sits. The excitation laser light is focused on the sample by an objective and the fluorescence light from the SiV centers collected by the same objective, hence the name confocal. The sample can be moved to scan it in order to excite emitters and collect the fluorescence light. For scanning, an avalanche photo diode is attached to the confocal setup.
- The grating spectrometer to investigate the spectral properties of the emitters. This is crucial to distinguish between SiV centers, other color centers and nanodiamonds which do not host color centers.
- A Hanbury Brown and Twiss (HBT) setup to investigate the single photon character. It is built up of two avalanche photo diodes (APDs) which are also used for scanning the sample and for performing saturation measurements.

saturation  
already  
introduced?

### 3.1 Confocal Setup

Figure 3.1 depicts a sketch of the confocal setup. Except for the laser and the sample stage, the whole setup is fixed to a vertical breadboard. As this vertical design permits a horizontal sample stage, it allows for easy scanning and exchanging of the samples, without the need of gluing them to a vertical stage. The friction between the sample and the aluminum surface of the stage is sufficient that the sample does not get out of place during scanning. For some measurements it is important that the sample has a defined orientation. For this purpose it is possible to orient it with the help of an aluminum angle and adjust the orientation with a

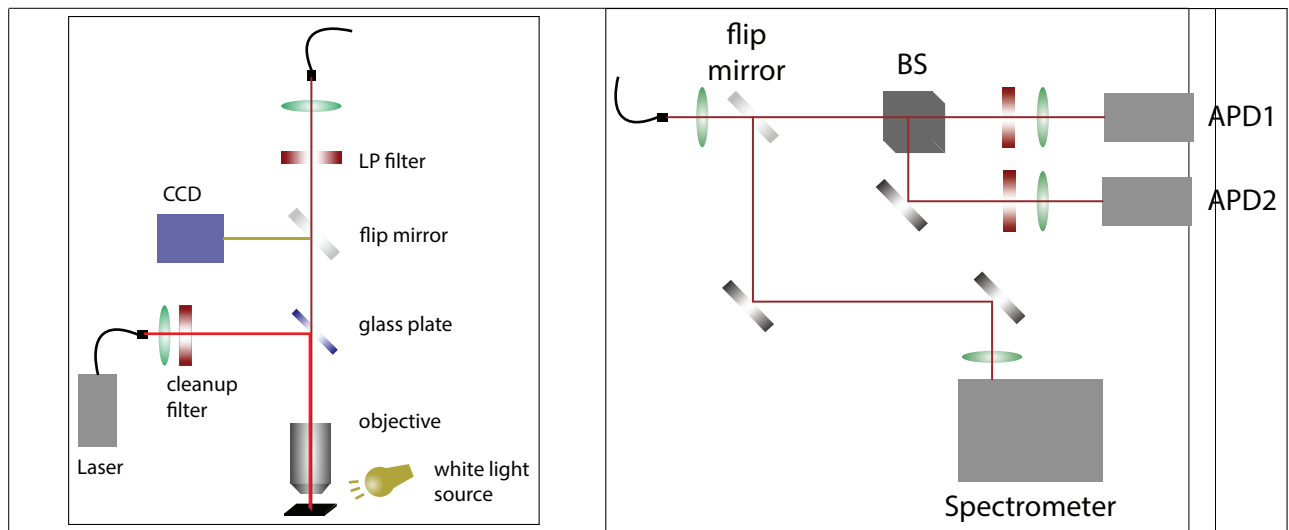


Figure 3.1: Confocal setup

Figure 3.2: HBT, spectrometer

manual rotation stage. In contrast, the translation stage is powered with two stepper motors (Newport MVP25XL) in the horizontal x and y directions. Above the horizontal stage, the objective is fixed to another stage which in turn is fixed to the vertical breadboard. In this way, the vertical z distance can be adjusted for focusing the laser light on the sample. It also enables scanning in the direction of the optical axis, which is coincides with the height of the sample. Therefore, three-axis scanning of the sample is implemented.

The bright red color in the sketch in Figure 3.1 represents the excitation beam path. The sample is excited with a continuous wave diode laser (Schäfter-Kirchhoff, 58FCM) which emits at a wavelength of 660 nm. The outlet of the laser is a pigtail fiber. The laser light is outcoupled and collimated exploiting an aspheric lens. To suppress sideband emission from the laser, a 660 nm bandpass filter with a filter window of 10 nm is used. After this cleanup filter, the excitation beam then hits a glass plate (fabricator Halle Germany) which guides the beam through a microscope objective to be focused on the sample. The microscope objective is of the type Olympus, LMPlanFLN 100x and has a numerical aperture of 0.8. As the luminescence light from the emitter is in the same focus as the excitation laser light, it is effectively collected by the objective (hence "confocal setup").

The collected light follows the detection beam path depicted in dark red in Figure 3.1. Both the excitation light reflected from the sample surface and the fluorescence light from the color centers pass through the glass plate. If the flip mirror behind the beamsplitter is taken out of the beam path, the beam is directed towards a single mode fiber which connects the confocal setup with either the spectrometer or the HBT setup. In front of the single mode fiber there is a longpass filter to filter out the residual excitation light and also ambient light. The filter is chosen with a cutoff wavelength of 710 nm or 720 nm. The fluorescence light is fed into the single-mode fiber (Thorlabs SM600) with an aspheric lens. Besides the obvious purpose of guiding the photoluminescence light to the spectrometer and the Hanbury Brown and Twiss setup for spectroscopic investigations, it has another crucial application: Its diameter of about 4.3  $\mu\text{m}$  serves as a pinhole to reject photoluminescence light from depths outside of the focal plane [4]. For this axis the resolution amounts to , in the plane of the sample it is .

thickness

value

value

short discussion if resolution is enough

According to the experimental necessities, instead of the mentioned glass plate a dichroic mirror (DRLP692) can be employed. The dichroic mirror spectrally separates excitation light from photoluminescence light as it selectively transmits and reflects sight as a function of its wavelength. The glass plate features a high transmission of 90% and therefore exhibits a high collection efficiency of fluorescence light, but at the same time, 90% of the excitation light is lost, as it is not reflected towards the sample. In contrast to that the dichroic mirror allows for a higher excitation intensity using the same excitation laser which is necessary for instance for saturation measurements. However, a high excitation intensity may cause permanent fluorescence intermittence of the SiV centers (for further detail, refer to ). In general, if a high excitation is necessary, as for saturation measurements, the dichroic mirror is used; otherwise, the glass plate is used to collect as much fluorescence light as possible without damaging the SiV centers due to exposure to a high laser light intensity.

## 3.2 Optical Imaging of The Sample Surface

The confocal can be modified to investigate the sample surface before starting the fluorescence measurements. For this purpose, the sample is directly illuminated in a flat angle from outside the objective with white light from a halogen lamp (depicted as white light source in Figure 3.1). The flip mirror behind the glass plate is brought into an upright position to guide the light towards a CCD camera (). The scattered light from the sample surface is collected by the objective and the surface is imaged on the CCD chip . Hence Nanodiamonds and other features on the substrate are visible. The resolution of this configuration of the setup is limited by .

In chapter ?? an application of the nanodiamond is introduced, for which it is of major importance to know the position of specific nanodiamonds. Therefore, cross markers are milled into the surface of the substrate on which the nanodiamonds are situated. These markers of a size of 10  $\mu\text{m}$  can easily be recognized by optical iamging. The starting point for a scan of an area of interest on the sample is fixed while navigating with the optical image. After flipping the flip mirror, a photoluminescence scan of that area is started.

## 3.3 Spectrometer

Figure 3.2 displays the detection part of the setup. The fluorescence light from the fiber which connects the confocal setup with the detection setup is outcoupled with an aspheric lens. A flip mirror is employed to direct the light either to a grating spectrometer or the HBT setup. The optical spectrum of a light source gives insight to the optically active constituents and therefore bears information about the emitter.

As mentioned before, the fluorescence light from the SiV centers is investigated with the grating spectrometer (Princeton Instruments Acton2500i). The incident beam passes through an entrance slit, is then scattered on the grating where the light is spectrally divided and finally hits a detector, imaging the entrance slit on the detector surface. The employed detector is a CCD camera () which is cooled with liquid nitrogen to a temperature of  $-120^\circ\text{C}$  for background reduction due to thermally generated free charge carriers. It is optimized for detection of light up to a wavelength of 900 nm. The spectrometer features three gratings: 600 grooves/mm, 1200 grooves/mm, and 1800 grooves/mm. These gratings are mounted on a

check  
number

insert  
chapter

specs

resolution  
CCD

optical  
diffrac-  
tion,  
shadows

type

turret, allowing easy switching of the gratings between measurements.

With the spectrometer's step-and-glue function which is implemented in the spectrometer software (WinSpec) it is possible, to record several spectra over a wide wavelength range which are then stiched together. It is therefore possible to combine a larger wavelength range with a higher resolution. For most measurements the grating with 600 grooves/mm was used. The resolution of the spectrometer using the 600 grooves mm<sup>-1</sup> is 0.13 nm at 738 nm and the accuracy amounts to  $\pm 0.4$  as stated by the manufacturer. This resolution suffices for most of the measurements mentioned in this work.

### 3.4 Hanbury Brown and Twiss Setup

A Hanbury Brown and Twiss setup serves to record the photon autocorrelation function ( $g^{(2)}$  function) of an emitter. In this work, the  $g^{(2)}$  function is used to make statements about whether a photoluminescence source emits single photons and is therefore one single emitter. In the photon number representation, it is defined as follows:

$$g^{(2)}(0) = \frac{\langle N(t)N(t + \tau) \rangle}{\langle N(t) \rangle^2}.$$

Here,  $N(t)$  denotes the photon at a certain time  $t$ ,  $N(t + \tau)$  denotes the photon at a time interval  $\tau$  later than  $t$ . The angular brackets  $\langle \rangle$  denote the temporal averaging. The physical explanation is that if the source is a single emitter and emits a photon at a time  $t$ , the next time any photon is recorded is at time  $t + \tau$ . For a time interval close to zero, the value of the  $g^{(2)}$  function must ideally approach zero or at least be smaller than 0.5 if only a single emitter is present: The denominator is zero, because  $N(t + \tau)(\tau = 0) = 0$  due to only one photon, namely  $N(t)$  being present. If two photons are emitted at the same time (time delay zero), the  $g^{(2)}$  function yields  $g^{(2)}(0) = 0.5$ . (For a detailed explanation of the  $g^{(2)}$  function read [5])

The principle of the HBT setup is to evaluate the time delay between two consecutive photons. A sketch of the HBT setup is shown in Figure 3.2. The photons are detected with single photon avalanche photo diodes (APDs) of the type PicoQuant  $\tau$ -SPAD100. APDs are the semiconductor analog to photomultiplier tubes: An incoming photon creates secondary charge carriers through ionization. The secondary charge carrier is accelerated by a bias voltage to create more secondary charge carriers, resulting in an avalanche effect. Therefore, the signal of a single photon is intensified and detected as an electrical current pulse. These avalanche photo diodes have a nominal detection efficiency of up to 70% at an optimal wavelength of about 670 nm and a dark count rate of under 100 cps. If a charge carrier created by the avalanche is trapped and later liberated, it induces a so-called afterpulse. To avoid detecting these artifacts as real events, the APDs have a dead time of about 70 ns. In the ideal case, one APD would be enough to measure the time delay between two consecutive photons. However, the second of two consecutive photons could hit the detector during its dead time. To circumvent this problem, two APDs are employed and the detection beam is split with a non-polarizing 50:50 beamsplitter cube. Each beam then passes through a bandpass filter and is focused on the avalanche photo diode with an aspheric lens. As the beam path is slightly different for each APD, a small optical path difference is introduced, however, this difference only results in an offset of the  $g^{(2)}$  function and does not alter the physical nature of the result. The bandpass filters serve two purposes: First, they limit optical crosstalk between

fox nach  
lesen

the avalanche photo diodes. The detection process in an avalanche photo diode produces light due to recombination of charge carriers. Crosstalk between two avalanche photo diodes occurs, if one of the photons produced by recombination in one avalanche photo diode escapes and is detected in the other one [6]. Secondly, the bandpass filters serve to reduce background during the  $g^{(2)}$  measurement process or to spectrally divide emission from several emitters. Therefore, it is possible to find single emitters, which are not spatially separated enough to be separated by the spatial resolution of the setup: They can be individually investigated if their ZPLs exhibit wavelengths which are spectrally well separated. Bandpass filters suited for the respective wavelengths are used to investigate light from one of the ZPLs.

When the APD fires, it outputs a digital TTL (transistor-transistor logic compatible) signal. The arrival times of the signals (so-called time tags) are recorded with a time tag unit (produced by dotfast-consulting, timing resolution 78.125 ps). The timing uncertainty of the photon detection process introduces variations of the digital signal's time tag from the actual detection time. Note that this error does not represent the time evolving from the photon impact to recording, but solely the uncertainty of the exact recording time. This process is called timing jitter. It affects the time tags and with them the physical nature of the  $g^{(2)}$  function. A discussion of the impact of timing jitter will be given in ??.

As stated earlier, the time delay between two consecutive photons is necessary for the reconstruction of the  $g^{(2)}$  function. The time delays are fed into a histogram which is then fitted to receive the continuous  $g^{(2)}$  function. In the Hanbury Brown and Twiss-setup the arrival time of the photons are measured with two APDs and for each APD one list of arrival times is recorded as raw data. To get a single array of arrival times of the photons, which can then be binned to obtain the  $g^{(2)}$  function, the arrays of time tags of the two APDs have to be correlated. For that, the time difference between each entry in one array and all consecutive time tags in the other array are determined and stored according a binning defined by the timing resolution of the time tag unit. After normalizing and fitting these data, statements about whether the emitter is a single emitter can be made.

wording

put in reference

---

---

## Chapter 4

# Fabrication of Nanodiamonds

“Diamond forms under high temperature and pressure conditions that exist only about 100 miles beneath the earth’s surface.” (Homepage of the Gemological Institute of America Inc.) While this statement is true for natural gem diamonds, various methods exist to synthetically produce diamond for applications in industry and research. In this chapter, different fabrication methods of diamonds and nanodiamonds in particular are explained. The first two procedures described are the high-pressure, high-temperature method and the chemical vapor deposition are described. These are two of the most commonly used fabrication methods for laboratory-produced diamonds. The high-pressure, high-temperature (HPHT) process mimics natural conditions under which diamond is formed within earth and is widely used to synthetically produce diamonds for industry. While these HPHT diamonds are exploited for some experiments reported in this work, most measurements which are subject in this thesis are carried out on diamond produced with a CVD process. The third method which is described is the wet-milling process in a vibrational mill, which is a technique using chemical vapor deposition or HPHT diamond. Nanodiamonds produced with this milling process are the main focus of this thesis. It has to be stressed, that in contrast to the first two methods described in this chapter, the wet-milling process is not a process to produce diamond itself, rather it serves to crush bigger diamond starting material into pieces of a desired size. For a more extensive list of diamond production processes refer to e.g. [7]. Aside from the general diamond fabrication processes, the production details of the nanodiamonds used for this thesis will be mentioned.

### 4.1 High-Pressure High-Temperature Diamond

The HPHT process was the first process to successfully synthesize diamond (in 1879). Temperatures of a few thousand degrees Celsius and pressures between 50 000 bar and 100 000 bar are needed [7]. Today, it is still widely used due to its relatively cheap production costs [8]. In the HPHT process, diamond is synthesized from graphite. The machine used for this kind of synthesis is a press. For some forms of this method, a metallic solvent is added which lowers the needed pressures; the solvent causes the graphite to dissolve at lower pressures and temperatures, and at the same time it causes the diamond to crystallize. Several press designs exist, which all provide a high temperature and a high pressure in their core. While it is possible to grow big ( $> 10$  carat) high-quality diamonds with the HPHT process, it is

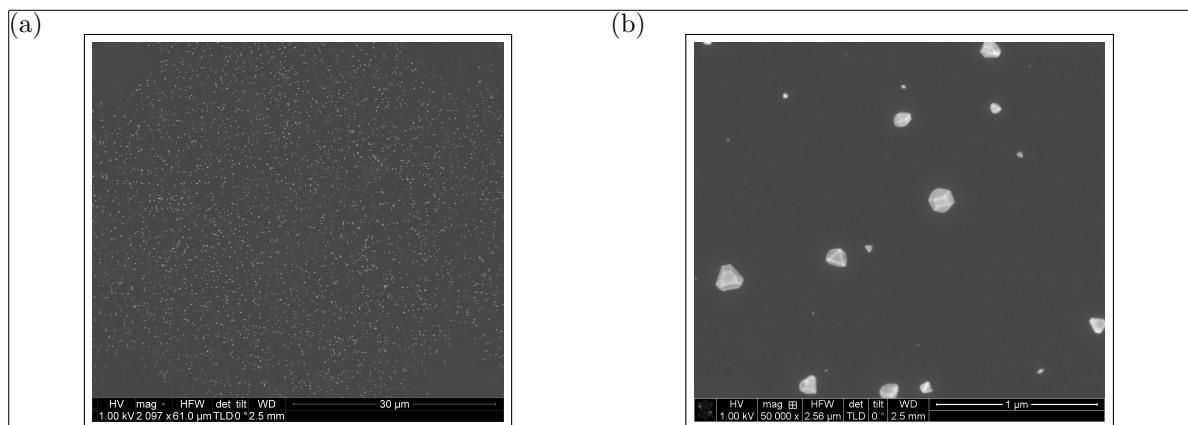


Figure 4.1: SEM images of CVD grown diamonds (sample insitucvd) produced by M. Schreck's group (Augsburg University). The average size of these nanodiamonds is 100 nm. (a) Overview image, white dots are nanodiamonds. (b) Detail image, it can be seen that not all nanodiamonds exhibit the same size and that they coexist in different shapes.

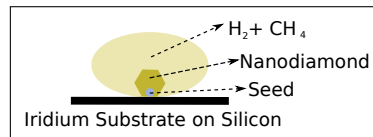


Figure 4.2: Sketch showing the production of CVD nanodiamonds in the growth chamber with a methane gas environment.

rather expensive when compared to the CVD process due to the necessary high temperatures and high pressures.

In the scope of this thesis, HPHT diamonds produced by Davydov et al. [9] are spectroscopically investigated.

sind die  
nicht  
auch zer-  
mahlen  
worden?

wie kom-  
men da  
die SiVs  
rein?

ueberleitu-  
zu naech-  
stem  
satz

## 4.2 Chemical Vapor Deposition Diamond

In contrast to the HPHT process, during the chemical vapor deposition process, diamond is grown from a vapor phase. This process requires moderate temperatures ( $700^{\circ}\text{C}$  to  $1300^{\circ}\text{C}$ ) but low pressures of less than 1 bar in a vacuum chamber [] The diamond in a metastable state Atomic hydrogen is necessary to suppress the simultaneous growth of graphite. The vapor phase within the growth chamber is a mixture of hydrogen and methane, the latter of which acts as a carbon source. Within the vacuum chamber, activation of the gas by an energy source (e.g. microwave plasma) breaks apart the gas molecules to release carbon atoms. These atoms are drawn down toward the cooler substrate. On the substrate surface, various processes occur, such as adsorption, desorption and diffusion. The growth parameters are optimized such that growth of diamond is favored with respect to graphite.

Growth on a substrate is easier, if the lattice constant of the substrate and the crystal to be grown are very similar. The lattice constant of iridium ( $0.384\text{ nm}$ [10, 11]) is very similar to the lattice constant of diamond ( $0.356\text{ nm}$ [12]). Therefore, the diamonds were grown on a stratified substrate, consisting of iridium layers of  $60\text{ nm}$  to  $150\text{ nm}$  thickness grown onto an

yttria-stabilized zirconia (YSZ) buffer layer, which in turn was grown on a silicon wafer [13]. If the lattice constant of the substrate and the diamond are not matched, stress in the diamond lattice is induced. Therefore, the iridium substrate not only facilitates diamond growth, but also reduces unfavorable stress in the nanodiamonds (more on the effect of stress in ??).

For crystals to form in heteroepitactic growth (i.e. one type of crystal is grown upon the surface of a different type), a nucleation step is necessary [14]. The easiest method to obtain nuclei on a substrate is to spin-coat the substrate with small diamond seed crystals of a size of a few nanometers. This method is exploited for all the CVD grown nanodiamonds investigated in this thesis. Such small seed diamond crystals are commercially available, and are usually diamond particles produced by a so-called detonation process. In a detonation process, the high pressure produced by shockwaves of a detonation is used to create very small diamond particles of a size down to a few nanometers. During the CVD growth process, carbon from the methane gas is adsorbed to the seed crystals. To produce nanodiamonds of a desired size, the growth process is stopped when the diamonds grown onto the seed crystals reaches the desired size. If the growth process is continued, the individual crystals grow together to form diamond films. Such diamond films are used as starting material for the wet-milling process described in the next section (section 4.3)

One of the advantages of the CVD process is that silicon is incorporated *in-situ*. This is achieved by etching of silicon substrate edges by the plasma which automatically occurs in the growth chamber and silicon atoms diffuse into the methane gas. For a higher silicon content in the diamond, sacrificial silicon is put into the growth chamber. These atoms are then built into the diamond lattice while growth.

After nanodiamond growth, the nanodiamonds are either investigated directly on the growth substrate or they are shaken off in an ultrasonic bath to obtain a solution which is coated onto other substrates for further measurements.

In this thesis, two types of samples were investigated which were directly produced as nanodiamonds.<sup>1</sup> The first batch (henceforth called CVD samples) were grown on detonation diamond seeds of a size smaller than 3 nm (produced by the company Microdiamant, product Liquid Diamond monocrystalline, MSY 0-0.03 micron GAF). For the growth process, 1% of methane is added to the hydrogen environment in the growth chamber. The growth process is performed with a pressure of 30 hPa for 30 min to 60 min, yielding nanodiamonds of a diameter of about 100 nm to 200 nm.

The other samples directly produced by a CVD process are nanodiamonds grown onto molecular analogs of diamond crystals. A subgroup of these molecular diamonds are called diamondoids and are carbon crystals based on the carbon cage molecule adamantine  $C_{10}H_{16}$ . The molecular diamonds used for this work are adamantine in cyclohexane, mercapto adamantine in cyclohexane, and cyclohexane. Each of these seed crystals is used in different growth processes. During the growth process, either 3% or 1% methane was added to the hydrogen plasma and either silicon or silicon dioxide was exploited to form *in-situ* incorporated SiV centers (see Table 4.1).

is this  
correct?

irgendwo  
einfue-  
gen, was  
ich dies-  
bezgl.  
gemacht  
hab

put in  
figure

### 4.3 Wet-Milled Nanodiamonds

Apart from growing nanodiamonds of a specific size directly via a CVD process, macroscopic diamond starting material can be crushed to obtain small diamond particles. In contrast

<sup>1</sup>The CVD nanodiamonds were grown by the group of M. Schreck [13].

Table 4.1: Summary of the samples grown on diamondoid seed crystals.

Sample name	Seed crystals	Methane conc.	Silicon source
160211_E	Mercapto adamentane in cyclohexane	1%	SiO <sub>2</sub>
160211_F	Cyclohexane	1%	SiO <sub>2</sub>
160212_C	Cyclohexane	3%	silicon
160212_D	Adamentane in cyclohexane	3%	SiO <sub>2</sub>
160212_E	Mercapto adamentane in cyclohexane	3%	SiOs
160212_F	Cyclohexane	3%	SiO <sub>2</sub>

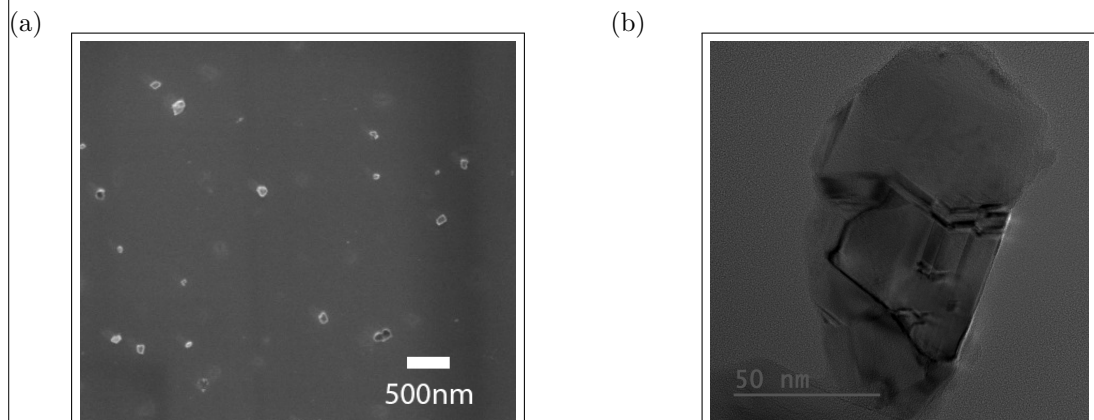


Figure 4.3: Pictures of the milled nanodiamonds (sample insitu100). (a) SEM picture showing the distribution of the nanodiamond crystals on the iridium substrate. (b) TEM picture of a nanodiamond particle.

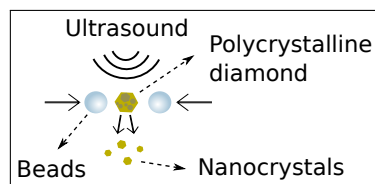


Figure 4.4: Sketch showing the wet-milling process in a vibrational mill. Vibrations from the mill drive the beads which collide with the diamond material and crush it to smaller pieces.

to nanodiamonds directly grown by a CVD process, the process is divided into two subprocesses: 1. Diamond is produced, for example by an HPHT process or by CVD growth. 2. The macroscopic diamond is milled to smaller diamond particles. For the wet-milling process which yields the nanodiamonds investigated in this thesis<sup>2</sup>, small beads are used to crush the diamond material. The beads are driven by vibrations of a vibrational mill. A sketch of the process is shown in Figure 4.4.

The big advantage of the milling process is that it enables the production of a large quantity of diamond nanoparticles. When producing nanodiamonds directly via a CVD process, the number of produced nanodiamonds in one process scales with the surface of the substrate on which the nanodiamonds are grown. In contrast, the quantity of milled nanodiamonds scales with the volume of the starting material. Therefore in one and the same process the limit for the obtainable amount of diamond nanoparticles is much higher. Another advantage of the milling process is that the nanodiamonds are in an aqueous solution after milling. Therefore, it is viable to spin-coat the nanodiamonds directly onto any substrate suited for further experiments without further treatment.

The wet-milled nanodiamonds have the disadvantage to contain grain boundaries, resulting in reduced crystal quality (Figure 4.3b). While the polycrystalline diamond film is more likely to break apart at grain boundaries, the final nanodiamonds still contain grain boundaries. In contrast, as-grown CVD nanodiamonds are mainly single crystals.

After milling, the nanodiamonds are treated with post-processing steps including annealing in vacuum and oxidation in air. A detailed description of the processes and their impact is given in 5.

In principle diamond produced by any production method can be used as starting material for the milling process. In the following sections, they are distinguished by the respective starting material and milling method.

### 4.3.1 Wet-Milled HPHT Nanodiamonds

We investigated nanodiamonds, which were produced from a HPHT starting material and milled by a wet-milling process to median sizes of about 45 nm, 80 nm and 260 nm. They were then drop-casted onto an iridium substrate and implanted with  $^{28}\text{Si}^{1+}$ <sup>3</sup>. At last, all HPHT nanodiamonds (samples hphtimp45, hphtimp80, hphtimp260) were oxidized in air at  $450^\circ\text{C}$  for 3 h.

### 4.3.2 Wet-Milled chemical vapor deposition Nanodiamonds

In the following paragraphs, details of the production processes of nanodiamond produced by wet-milling a CVD diamond film in a vibrational mill are described. For an overview of the samples refer to Table 4.2. The starting material for the wet-milled nanodiamonds was a nanocrystalline diamond film [15] directly grown on a silicon wafer by CVD. A microwave hydrogen plasma containing 1% methane was used to grow on purified 5 nm nanodiamond seeds

<sup>2</sup>If not otherwise stated, all the mentioned wet-milling processes were carried out by Andreas Muzha in the group of A. Krueger (Julius-Maximilians Universität Würzburg))

<sup>3</sup>Implantation was performed by Dr. Detlef Rogalla at Ruhr-Universität Bochum (RUBION - Zentrale Einrichtung für Ionenstrahlen und Radionuklide)

info  
about vibrational mill

more info

besser  
formulieren

etwas anders formulieren

implantati  
paramete  
ters

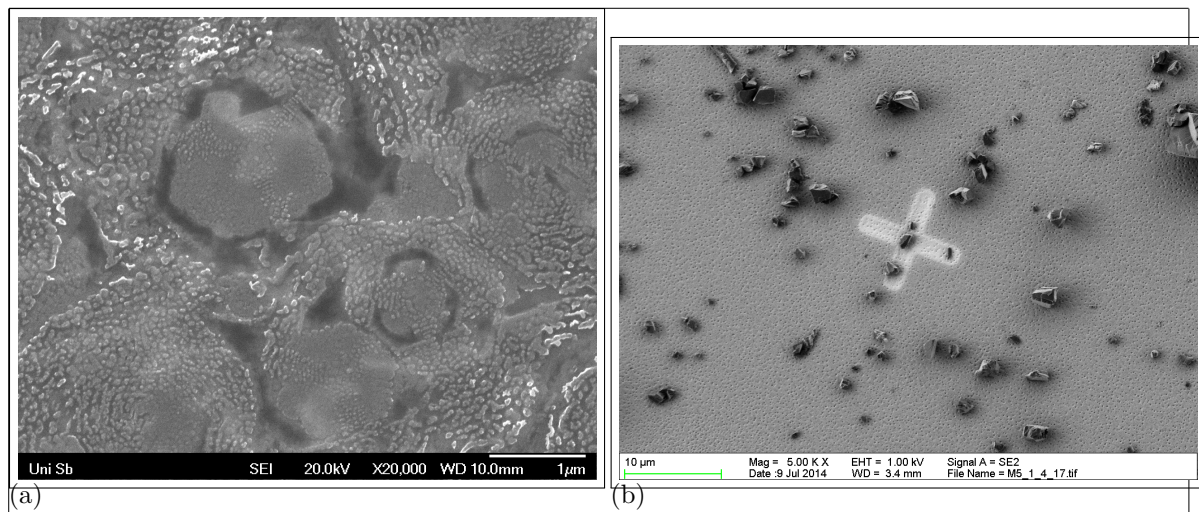


Figure 4.5: (a) SEM picture of nanodiamonds sunken into a silicon substrate after annealing at 900 °C for 3 h. Magnification 20 000. (b) SEM image of the microdiamonds after milling on an iridium substrate, but before implantation. In the middle of the picture, there is a reference cross milled into the iridium substrate with a focused ion beam. Its size amounts to 10  $\mu\text{m}$ . It can be seen, that the microdiamonds exhibit sizes of a few micrometer.

(produced by PlasmaChem). To induce *in-situ* SiV center creation, sacrificial Silicon pieces are situated in the growth chamber. During diamond growth the silicon pieces are etched by the plasma and individual atoms are incorporated into the diamond lattice. The diamond film is then milled by a wet-milling process in a vibrational mill with steel beads. The high amount of steel containment due to the steel beads is removed by extensive acid treatment. We also investigated nanodiamonds milled with silicon nitride beads, and found that the choice of material of the beads does not cause any spectroscopic difference ???. The median diameters of the diamonds are 50 nm, 70 nm and 100 nm (Figure 4.3a). The particle sizes are determined with laser diffraction spectroscopy. Transmission Electron Microscopy (TEM) pictures of the diamond crystals show that the milled nanodiamonds are polycrystalline, exhibiting a typical size of single crystals of a few tens of nanometers. In Figure 4.3b a TEM image of a typical nanodiamond is shown. Crystal boundaries have effects on the formation of color centers: SiV centers are more prone to form at crystal boundaries [16]. The aqueous solution containing the nanodiamonds is drop cast onto an iridium film on a Silicon substrate. The iridium film of a thickness of 130 nm is grown onto a buffer layer of yttria-stabilized zirconia (YSZ) which in turn is grown onto a Silicon wafer. The iridium surface has the advantage that it acts as an antenna and therefore enhances the collection efficiency of fluorescence light [17] (for more information on the substrate see section 4.4). Post-procession treatment comprises either both annealing in vacuum at 900 °C and consecutive oxidation in air at a temperature of 450 °C, or only one of the two methods. The duration for either treatment method was 3-6 hours.

### 4.3.3 Doubly Wet-Milled Implanted Nanodiamonds Implanted With Silicon

We also investigated nanodiamonds with SiV centers implanted after diamond growth. Starting material was a polycrystalline Element Six diamond film (electronic grade). In bulk material, the implantation causes the SiV centers to form in a specific depth dependent on the implantation energy, leaving most of the diamond vacant of SiV centers. As a consequence, a big portion of nanodiamonds milled from such a bulk material would not host any SiV centers. To obtain diamond particles with a homogeneous distribution of SiV centers, the process of fabricating implanted nanodiamonds is the following. First, the diamond film is milled to diamond particles of sizes of a few micrometers. In the second step, these microdiamonds are then spin-coated onto iridium substrates and implanted with  $^{28}\text{Si}^{1+}$ . To eliminate lattice damage and vacancies formed by the implantation process, the diamonds were annealed in vacuum and subsequently oxidized. At last, the micrometer sized diamond particles are milled to smaller sizes.

#### Preliminary Tests

The starting material was an Element Six electronic grade diamond film. The diamond was milled in a wet-milling process to sizes on the order of micrometers, which were then coated onto a silicon substrate. The microdiamonds were implanted with  $^{28}\text{Si}^{1+}$  at an implantation energy of 1.7 MeV, and fluences of  $10^9 \text{ cm}^{-2}$  to  $10^{12} \text{ cm}^{-2}$ <sup>4</sup>. After implantation, the microdiamonds on the silicon substrate were annealed for 2 h at 900 °C and oxidized in air for another 2 h at 450 °C. However, we encountered the problem that the silicon sublimated and re-nucleated during annealing, causing the diamonds to sink into the silicon surface (Figure 4.5a). Iridium is less prone to damage by high temperatures and withstands annealing procedures up to our standard annealing temperature of 900 °C without problems. Therefore, we used a sample with microdiamonds on a silicon substrate which was not annealed to shake the nanodiamonds off the silicon substrate in an ultrasonic bath, and consecutively coated the microdiamonds on an iridium substrate. After annealing and oxidizing the nanodiamonds on the iridium substrate, the iridium surface was intact.

#### Final Procedure

For the milling process in a vibrational mill, a minimum amount of diamond material is necessary. When starting with a diamond film, this threshold is easily reached, however, a big quantity of microdiamonds is needed to meet the requirements. Therefore, production was carried out at a larger scale after the preliminary tests. The microdiamonds were directly spin-coated onto iridium substrates, implanted with  $^{28}\text{Si}^{1+}$  (implantation energy 900 keV, fluence  $10^{11} \text{ cm}^{-2}$ )<sup>5</sup>. The microdiamonds were then annealed in vacuum for 3 h at 900 °C and oxidized in air for 3 h at 450 °C. At last, they were milled again to sizes of about 40 nm, 45 nm, 240 nm and 260 nm. The diamonds of sizes 40 nm and 240 nm were annealed in vacuum at 1200 °C.

how  
much?

time?

<sup>4</sup>Implantation performed by Dr. Detlef Rogalla at RUBION - Zentrale Einrichtung für Ionenstrahlen und Radionuklide, Ruhr-Universität Bochum mbH.

<sup>5</sup>Implantation performed by Jan Klug at rubitec - Gesellschaft für Innovation und Technologie der Ruhr-Universität Bochum mbH.

Table 4.2: Summary of the wet-milled samples. The first column indicates the names of the samples, the second the mean diameter of the nanodiamonds, and the third describes how the silicon was incorporated into the diamond.

Sample name	Size	Si incorporation	Post-processing
hphtimp45	45 nm	<i>implanted</i>	oxidized in air at 450 °C
hphtimp80	80 nm	<i>in-situ</i>	annealed in vacuum for 1 h at 1000 °C and at 900 °C for 3 h
hphtimp260	260 nm	<i>in-situ</i>	oxidized in air at 450 °C
insitu50	50 nm	<i>in-situ</i>	series of individual samples with diverse post-processing steps
insitu70	70 nm	<i>in-situ</i>	series of individual samples with diverse post-processing steps
insitu70n	70 nm	<i>in-situ</i>	no post-processing subset of insitu70
insitu70o	70 nm	<i>in-situ</i>	oxidized in air at 450 °C subset of insitu70
insitu100	100 nm	<i>in-situ</i>	series of individual samples with diverse post-processing steps
insitu100ao	100 nm	<i>in-situ</i>	annealed in vacuum at 900 °C, consecutively oxidized in air at 450 °C subset of insitu100
implanted250ao	250 nm	implanted	annealed in vacuum at 900 °C, consecutively oxidized in air at 450 °C
hphtimp260	40 nm	implanted	annealed in vacuum at 1200 °C, consecutively oxidized in air at 450 °C
hphtimp260	50 nm	implanted	oxidized in air at 450 °C
hphtimp260	240 nm	implanted	annealed in vacuum at 1200 °C, consecutively oxidized in air at 450 °C
hphtimp260	260 nm	implanted	oxidized in air at 450 °C

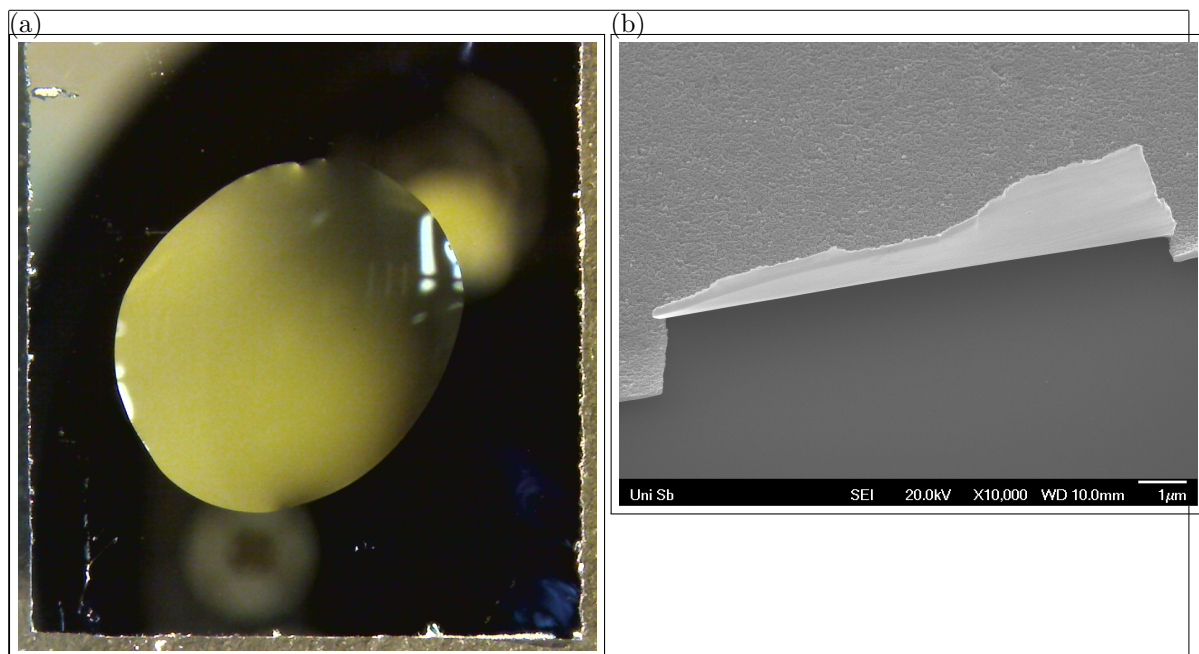


Figure 4.6: (a) Microscope image of a drop of water on an iridium substrate cleaned with Piranha etch. This picture was used to estimate the contact angle. (b) SEM picture of an 60 nm iridium layer that peeled off the substrate after an ultrasonic bath.

## 4.4 Iridium Substrate

As mentioned in section 4.2, we used a silicon substrate with an iridium layer on top for most experiments in order to match the lattice constant of diamond. We also use the same substrates for the experiments with wet-milled diamonds, as the iridium exhibits further advantages:

- The high hydrophilicity of iridium enhances the homogeneity of the nanodiamonds on the substrate after spin-coating or drop-casting. The hydrophilicity is further improved by treating the substrate in a Piranha etch (50:50 mixture of sulfuric acid  $H_2SO_4$  and hydrogen peroxide  $H_2O_2$ ) by removing oxide layers on the surface. The treatment with Piranha etch also has the advantage that all organic contamination is removed. Measurements after applying the Piranha cleaning yielded an estimation of the contact angle of slightly more than one degree. To determine the contact angle with water, the volume of a water drop is compared to the surface it covers after dropping it onto an iridium substrate. From that an estimation of the contact angle is deduced.
- During the post-processing steps, it is of major importance, that the substrate can withstand high temperatures. As described in section 4.3.3 during the preliminary tests with implanted nanodiamonds on a silicon substrate (sample name  , we encountered difficulties with diamonds on a silicon substrate as the sunk into the surface after annealing. In contrast, iridium withstands the used annealing process without damage.
- Additionally to the mentioned technical advantages, another advantage of the iridium surface manifests itself during spectroscopic measurements: Iridium acts both as a mirror and as an antenna for the fluorescence light emitted by the SiV center [17].

check  
numbers

sample  
name

Therefore, the collection efficiency of the fluorescence light is enhanced.

These advantages of iridium surfaces are only countered by one minor disadvantage: If the iridium layer is too thin, it tends to peel off the substrate (Figure 4.6b). We encountered this problem during a cleaning procedure in the ultrasonic bath. However, this disadvantage is easily circumvented by using a thicker iridium layer. For our measurements, we used an iridium layer of a thickness of 130 nm, with which we did not encounter any adhesion problems.

#### 4.4.1 Preparation of The Substrate

Prior to drop casting, the substrate is cleaned. The standard cleaning procedure comprised the following cleaning steps in an ultrasonic bath (3 min to 7 min each):

- Distilled water with a drop of dishwasher detergent
- Isopropanol (99.9% p.a.)
- Acetone (99.9% p.a.)
- Distilled water

Thereafter, the substrates are put into a Piranha solution (50% sulfuric acid  $H_2SO_4$ , 50% hydrogen peroxide  $H_2O_2$ ) to enhance the surface hydrophilicity and therefore obtain a homogeneous distribution of diamonds on the surface. They are then put again into distilled water and blown dry with compressed air to avoid residue from the water. The substrates were then either drop-casted or spin-coated with aqueous diamond solutions. For the prior, the substrates are heated to a temperature of 60 °C and drops of a volume of about 5  $\mu L$  dropped onto the substrate. If substantially more than 5  $\mu L$  is needed, the several drops of about 5  $\mu L$  are dropped onto the substrate consecutively, as with a single big drop the solution would flow off the substrate before drying. For spin-coating, a home built spin coater was used. Drops of 5  $\mu L$  are dropped on the substrate and the spin-coater set to a velocity of 2500 rpm for 3 min.

## Chapter 5

# Crystal Quality of Nanodiamonds

Crystal quality is the a measure for how close a crystal resembles its pristine form []. Vacancies, impurity atoms and inclusions of graphite or amorphous carbon are examples for factors which decrease the crystal quality ?? . Poor crystal quality manifests itself in photoluminescence spectra e.g. as broad spectral background fluorescence. To improve crystal quality, two methods are used: annealing in vacuum and oxidation in air. We investigated the effect of oxidation on the Raman spectrum. Raman measurements of various samples give insight to crystal quality and surface contamination. Additionally, several TEM measurements exhibit the composition of the wet-milled nanodiamonds.

### 5.1 Annealing and Oxidation

During silicon implantation the diamond lattice gets damaged by the penetrating ions.  $sp^2$  bonds, carbon interstitials and vacancies disrupt the metastable equilibrium of the diamond phase. Hence, there is a tendency for damaged diamond to "tip over" to the thermodynamically stable form of carbon, i.e. graphite. At temperatures above about  $500\text{ }^\circ\text{C}$ , vacancies in the diamond lattice become mobile and diffuse towards the surface[18]. Literature suggests, that annealing at  $900\text{ }^\circ\text{C}$  for 1 h is sufficient to remove most of the damage following implantations, that however some damage remains even after annealing at  $900\text{ }^\circ\text{C}$  for 1 h. To reduce the damage in the diamond lattice, we anneal the implanted diamonds at  $900\text{ }^\circ\text{C}$  to  $1200\text{ }^\circ\text{C}$  for 3 h to 6 h in vacuum ( $10^{-6}\text{ Pa}$ ).

The surface of the nanodiamonds is contaminated with graphite and amorphous  $sp^2$  hybridized carbon . The vacancies which diffuse towards the surface during annealing further increase the amorphous carbon content on the surface of the nanodiamonds []. We apply oxidation in an oven under ambient air at a temperature of  $450\text{ }^\circ\text{C}$  for 3 h to 6 h.

another citation

warum

### 5.2 Raman Measurements

Raman measurements of the wet-milled nanodiamonds give insight to the issues of surface contamination, defects in the diamond lattice and strain in the lattice: Surface contamination like graphite and amorphous  $sp^2$  hybridized carbon atoms cause additional peaks in the Raman

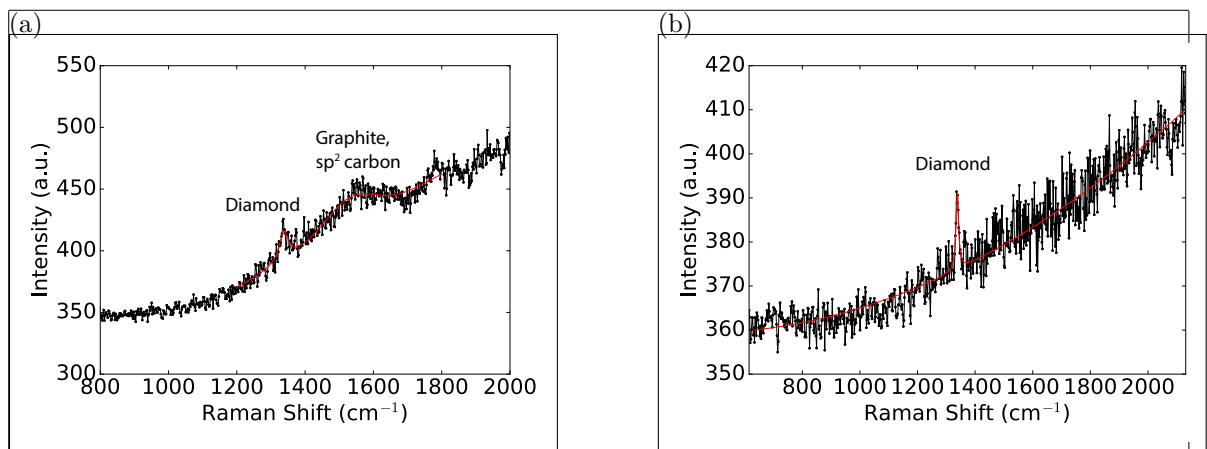


Figure 5.1: Raman measurements, black: data, red: fit. (a) Raman measurement before oxidation, sample insitu70. The diamond Raman peak is situated at  $1338\text{ cm}^{-1}$ . The broad feature around  $1600\text{ cm}^{-1}$  corresponds to the graphite G-band. (b) Raman measurement after oxidation, sample insitu70o. The G-band has vanished, indicating removal of graphite and amorphous  $\text{sp}^2$  hybridized carbon.

spectrum. A high defect concentration may lead to both additional peaks, to a broadening of the first order Raman peak and a shift to smaller wavenumbers. Strain in the diamond broadens the first order Raman peak and causes a shift to higher wavenumbers [19, 20, 21]. For the Raman measurements the same layout of the setup described in ?? is used. As excitation lightsource, a 532 nm continuous wave diode laser is used (IO ). It provides single (frequency) mode laser light, which is a prerequisite for Raman investigations. The beam-splitter is a dichroic mirror (DRLP645), the laser light is additionally filtered out with a 532 Notch filter in the detection path in front of the single mode fiber instead of the otherwise used longpass filter. With these adaptions, the combination of the confocal unit and the spectrometer serve as a Raman spectrometer. As the diamond Raman line is very narrow ( xx), the 600 grooves/mm grating is used for a first overview; for more detailed measurements the 1200 grooves/mm and 1800 grooves/mm gratings are used.

Due to the low signal from a single nanodiamond, the Raman measurements are carried out at several areas on the sample insitu70 which are densely covered with nanodiamonds, hence taking measurements of clusters of nanodiamonds. The narrow peak in Figure 5.1a corresponds to the first order diamond Raman peak. The Raman shift of  $1338\text{ cm}^{-1}$  compared to the literature value of  $1332\text{ cm}^{-1}$  of pristine diamond [19] indicates the presence of strain in the diamond particles. Furthermore, the investigated Raman spectra show a broad peak with a Raman shift of about  $1582\text{ cm}^{-1}$  (Figure 5.1a). This shift corresponds to the G-band due to amorphous  $\text{sp}^2$  hybridized carbon atoms and graphite. The exact G-band position and linewidth is sensitive to parameters such as the clustering of the  $\text{sp}^2$  phase, bond-length and bond-angle disorder, presence of  $\text{sp}^2$  rings or chains, and the  $\text{sp}^2/\text{sp}^3$  ratio [22].

Nanodiamond Raman spectra are considerably modified after oxidation in air at  $450^\circ\text{C}$ . To verify this, we perform Raman measurements on three different spots on a non-oxidized sample (insitu70), and for comparison on three different spots on a sample produced in the same process which is additionally oxidized. While the G-band peak is present in every measurement performed on the sample which was not oxidized, it is not present in any of the measurements performed after oxidation (Figure 5.1b), indicating successful removal of  $\text{sp}^2$

type

check  
number

hybridized carbon and surface graphite. The position of the diamond Raman peak is the same oxidized (*insitu*70o) and non-oxidized (*insitu*70n) samples, indicating no effect on strain in the diamond. On the other hand, the width of the diamond Raman peak is between  $15\text{ cm}^{-1}$  and  $30\text{ cm}^{-1}$  without oxidation treatment, but is only  $9\text{ cm}^{-1}$  to  $11\text{ cm}^{-1}$  after the oxidation process. A possible reason for a change of the width is improved crystal quality. This effect is also subject in the following paragraphs and will be explained in more detail there. For comparison, measurements of the Raman line were also carried out on the implanted sample implanted250ao. These diamond particles are big enough to perform measurements on single nanodiamonds. We found one diamond Raman line at  $(1308 \pm 5)\text{ cm}^{-1}$ , one at  $(1345 \pm 5)\text{ cm}^{-1}$  and one at  $(1348 \pm 5)\text{ cm}^{-1}$  (given uncertainties are governed by spectrometer resolution). We have to distinguish two cases, a shift of the first order Raman line to higher versus lower wavenumbers than the first order Raman line of  $1332\text{ cm}^{-1}$  in pristine diamond.

As mentioned before, a Raman shift of the first order Raman line to lower wavenumbers and a broadening of the Raman line indicates defects in the diamond lattice [20]. The Raman line at  $(1308 \pm 5)\text{ cm}^{-1}$  exhibits a broad linewidth of  $(25 \pm 5)\text{ cm}^{-1}$ . Therefore both the position and the linewidth of the Raman line indicate that there are many defects present in the diamond. The other case is a shift of the first order Raman line towards higher wavenumbers. The shift of the first order Raman line to higher wavenumbers is attributed to strain in the diamond lattice. While under hydrostatic pressure, the triply degenerate first order Raman peak remains degenerate, under uniaxial and more complex stress configurations (biaxial stress, shear stress etc.) mode splitting occurs [20]. As the measured peaks at wavenumbers higher than the wavenumber in pristine diamond are broad, we attribute these peaks to stress configurations other than hydrostatic stress, where the mode splitting manifests itself in a broadening of the peak due to limited spectrometer resolution.

To summarize, there are two cases, one where the first order Raman line hints at many defects present in the diamond lattice and the other that leads to the assumption that the stress configuration in the diamonds are uniaxial or more complicated stress configurations. In subsection 6.0.1 we will show that both of these assumptions fit nicely to the results from the measured photoluminescence spectra.

### 5.3 Transmission Electron Spectroscopy Measurements

We performed transmission electron microscopy (TEM) measurements to further investigate the crystal quality<sup>1</sup>.

---

<sup>1</sup>TEM measurements performed by J. Schmauch, group xxx

---

---

## Chapter 6

# Spectral Distribution of SiV centers in Nanodiamonds

In the following chapter, spectroscopic measurements of the SiV centers are described. At first, a short introduction will be given. The additional theory, which goes beyond the scope of the explained theory in chapter 2 and additional experimental equipment will be explained.

### 6.0.1 Photoluminescence spectra

To find nanodiamonds containing SiV centers on the substrate, confocal scans are performed. The SiV centers are further investigated by measuring photoluminescence (PL) spectra, single photon statistics and photostability. To reduce bias in the measurements, not only the brightest spots are investigated, but also those which are hardly brighter than background fluorescence. The luminescence spectrum of an SiV center is composed of a prominent zero-phonon-line and weak sidebands. Investigations of both are reported independently in the following paragraphs.

#### Zero-phonon-line

The center wavelength and the linewidth of the zero-phonon-line of each measured SiV luminescence spectrum of the samples insitu50, insitu70, and insitu100 are determined by fitting a Lorentzian fit to the ZPL. Both spectra from single and multiple SiV centers are taken into account. The linewidth of each ZPL is plotted against its center wavelength (Figure 6.1). What immediately strikes the eye is a pattern that to our knowledge has not been reported to date: The observed ZPLs accumulate in two different regimes, namely a horizontal lobe (denoted group H) and a vertical lobe (group V) divided by a gap with hardly any data points. Single emitters are found both in group H and group V (for more details about single emitters see section ??).

The two groups are defined by their characteristic center wavelengths and linewidths: In group H very prominent ZPL peaks are found which show linewidths between about 1 nm to 5 nm at center wavelengths which vary between about 715 nm to 835 nm. Figure 6.2a shows a representative spectrum of a single emitter of group H (denoted emitter H1), exhibiting

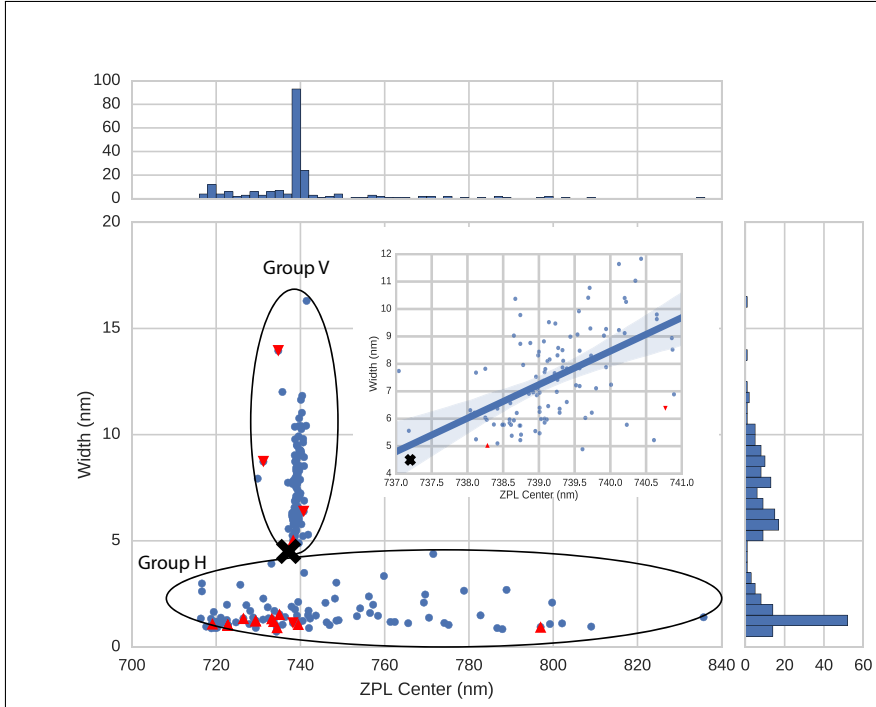


Figure 6.1: Distribution of the linewidth vs. the center wavelength of the ZPL of the investigated SiV centers in milled nanodiamonds containing *in-situ* incorporated SiV centers (samples insitu50, insitu70, insitu70n, insitu70o, insitu100). The data can be coarsely separated into two groups, H and V. The cross marks the position of an ideal SiV center in unstrained bulk diamond [23]. The red triangles indicate emitters which exhibited an antibunching dip in the  $g^{(2)}(0)$  measurement. Upwards pointing triangles represent emitters which exhibit fluorescence intermittency (blinking), while triangles pointing down represent emitters which do not exhibit any blinking (see subsection 6.1.1). The inset displays a zoom into group V, a least squares linear regression to the data, and the 95% confidence interval of the regression as a shaded area around the fit line. A clear trend of broader linewidths for longer ZPL center shifts is visible.

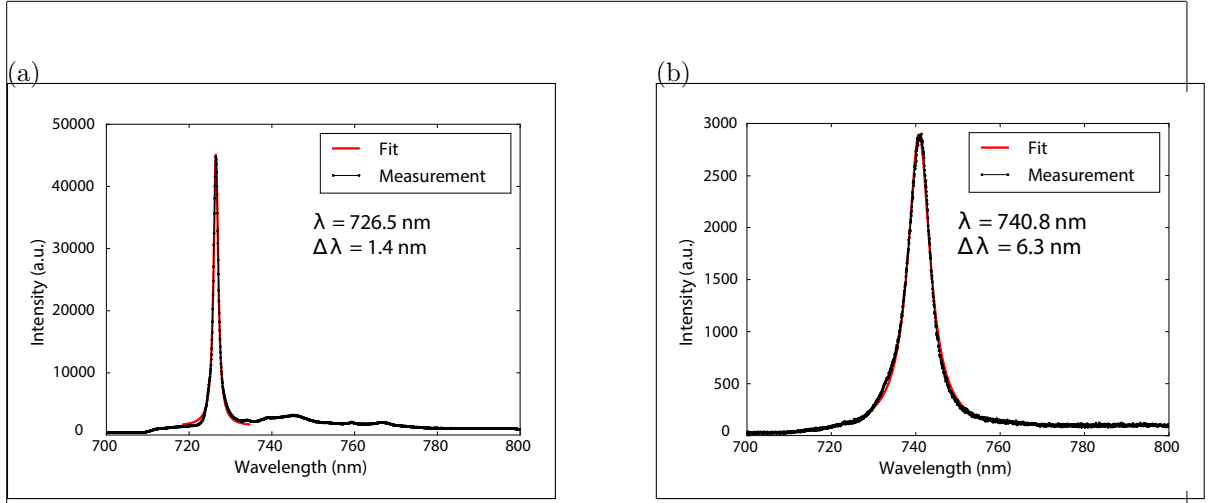


Figure 6.2: PL spectra measured with sample insitu100ao. (a) A representative room temperature spectrum of one of the emitters in group H of Figure 6.1, denoted emitter H1. (b) A representative room temperature spectrum of one of the emitters in group V of Figure 6.1, denoted emitter V1. The red lines are Lorentzian fits to the peaks.

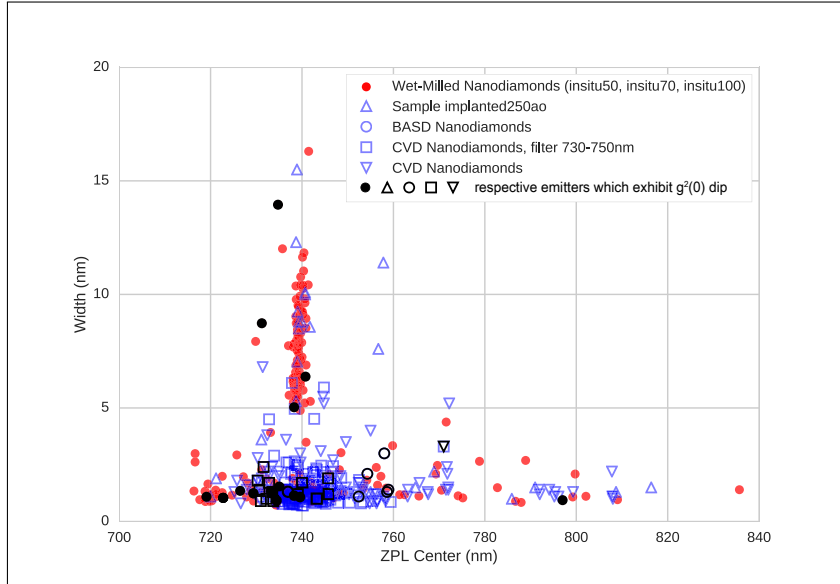


Figure 6.3: Comparison of the distribution of the linewidth vs. the center wavelength of the ZPL of the investigated SiV centers in milled nanodiamonds with data measured on the same nanodiamonds reported by J. Benedikter in [24], with data measured on CVD nanodiamonds, with data measured in CVD diamonds by E. Neu in a filter window between 730 nm and 750 nm [25], and with data measured on implanted250ao, implanted with Silicon. Black symbols represent emitters exhibiting a dip in the  $g^2(0)$  function, indicating a single or very few SiV centers

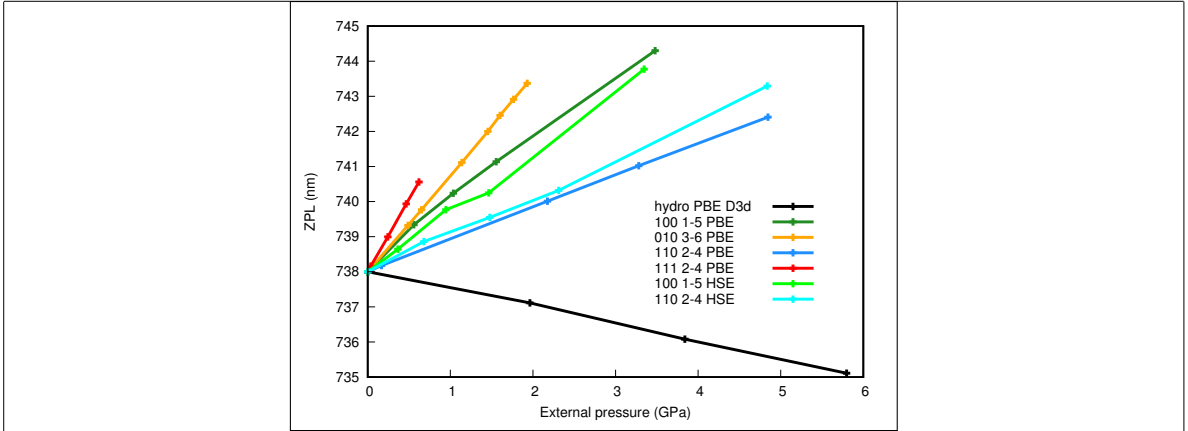


Figure 6.4: Calculations of the wavelength of the SiV center ZPL in dependence of pressure. Black: hydrostatic pressure; other colors: uniaxial pressure, for different orientations and calculated with different functionals PBE and HSE. Hydrostatic-type pressure causes a moderate blue shift whereas uniaxial strain causes larger redshift with different magnitudes depending on the direction of the strain [better description from Adam Gali](#)

a ZPL line width of 1.4 nm at a center wavelength of 726.5 nm. In contrast, in group V, the spectra exhibit broader ZPL linewidths of about 5 nm up to 18 nm. Their ZPL center wavelengths, however, are distributed within a very narrow range between 738 nm to 741 nm. Figure 6.2b shows a spectrum of a single emitter of group V (denoted emitter V1), exhibiting a ZPL linewidth of 6.4 nm at a center wavelength of 740.8 nm. For comparison, the room temperature ZPL of SiV centers in unstrained bulk diamond shows a linewidth of 4 nm to 5 nm at a center wavelength of 737.2 nm marked with a cross in Figure 6.1 [23, 26].

We also investigated the Debye-Waller of the reported spectra, which states the amount of emission light stemming from the ZPL wrt. emission from sidebands. The Debye-Waller of emitter H1 amounts to  $0.81 \pm 0.01$ , corresponding to a Huang-Rhys factor of  $0.21 \pm 0.01$  which is in good agreement with the values reported in [27]. The error is mainly due to background correction. When zooming in to the spectrum of emitter V1 it shows, that it does not exhibit any sidebands, i.e. all emission goes into the ZPL. Considering resolution limits of the spectrometer, the Debye-Waller factor amounts to close to 100%. It has to be pointed out, that we did not find any systematic difference of the Debye-Waller factor between group H and group V.

As the broad ZPL distribution shown in Figure 6.1 is unreported so far, we compare the results both to previous measurements and a control sample fabricated by silicon implantation. The comparison of current, earlier and control data is presented in Figure 6.3. Samples for which previous data has been taken are:

1. nanodiamonds produced by bead-assisted sonic disintegration (BASD) of polycrystalline CVD diamond films ([28]; data taken from [24])
2. nanodiamonds produced directly via a CVD process with *in-situ* incorporated SiV centers; measured in a spectral filter window of 730 nm to 750 nm (data reused from [25] with permission)
3. nanodiamonds produced in the same manner as the sample above; spectroscopic measurement procedure the same as the one performed on the milled, *in-situ* implanted

samples (see Table 4.2, insitu50 etc.)

All previous data from different nanodiamond material fit nicely with the ZPL distribution. To rule out that the two lobes in the distribution are no artifacts due to other elements incorporated into the nanodiamonds during the process, such as residue from other processes performed in the growth chamber or material abrasion from chamber parts and to verify that the observed luminescent defects are indeed silicon related, we performed control experiments that were implanted with silicon to form SiV centers (sample implanted250ao). Figure 6.3 shows that the implanted SiV centers cover roughly the same spectral range as the grown-in centers, thereby providing strong evidence for the silicon related origin of the defects.

In the next paragraphs, the ZPL distribution will be discussed in further detail. At first, the ZPL center wavelength shift is investigated. Very few of the measured data points in group V sit at a shorter center wavelength than the point attributed to an ideal SiV center in unstrained bulk material. This means, a red-shift of the ZPL of an SiV center is more likely than a blueshift. Several mechanisms contribute to the center wavelength shift, namely hydrostatic- and material strain. As explained in ??, we measured the Raman shift of samples insitu70 and implanted250ao. These measurements indicate strain in the diamond lattice. Figure 6.4 shows the calculated shift of the ZPL in dependence of pressure in the diamond lattice both for hydrostatic stress and for uniaxial stress. PBE and HSE are two different functionals used for the calculations . From Figure 6.4 it can be seen, the assumption stated in ?? that the strain in the nanodiamonds is mainly due to uniaxial stress corresponds well with the measured ZPL red-shift in group V. With higher uniaxial pressure, the ZPL becomes more and more red-shifted. However, the measured shifts in group H are too broad to be solely explained by strain in the diamond. We suspect that there are other defect sites present in the vicinity of the SiV center which explain the strong variation [29]. This statement is strengthened by the measurement of the shift of the first order Raman peak to lower wavenumbers. The investigation of this hypothesis presents an interesting topic for further research.

Zooming in to group V, another effect becomes visible (inset in Figure 6.1): With increasing ZPL, the linewidth becomes broader. The data points in group V are fitted with a linear regression to guide to the eye. Linking the correspondence between the strain and the redshift of the ZPL with that of the slope of between the center wavelength of the ZPL and the linewidth leads to the conclusion that also the linewidth is affected by strain in the diamond lattice: The higher the uniaxial stress, the bigger the linewidth.

To conclude, we are able to explain group V very consistently with theoretical predictions for the ZPL center wavelength shift due to strain in the diamond lattice. On the other hand, we suspect that group H is due to lattice defects in the vicinity of the SiV center, which has to be investigated in further research.

## Sideband

From literature it is known, that the SiV center in nanodiamond exhibits a large Debye-Waller of over 70% [30, 27], which is consistent with our measurements of emitter H1 and emitter V1. Nevertheless, sideband peaks are present in many SiV center PL emission spectra. The investigated emitters exhibit two different structures of sideband spectra: The spectra in group V exhibit one strong sideband peak (Figure 6.6), spectra in group H exhibit several weaker sideband peaks.

However, there is no recurring pattern in the sideband of group H. The challenge arises to un-

input  
Adam  
Gali

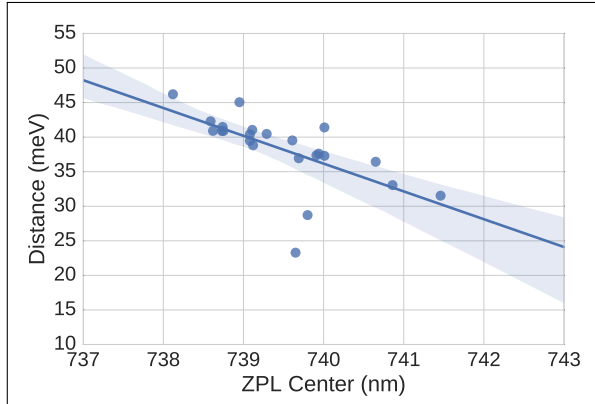


Figure 6.5: Shift of dominant sideband peak from the ZPL in spectra of SiV centers (group V, samples insitu50, insitu70, insitu100) vs. ZPL center wavelength. The linear fit shows that the shift decreases with increasing ZPL center wavelength. The shaded area is the 95% confidence interval.

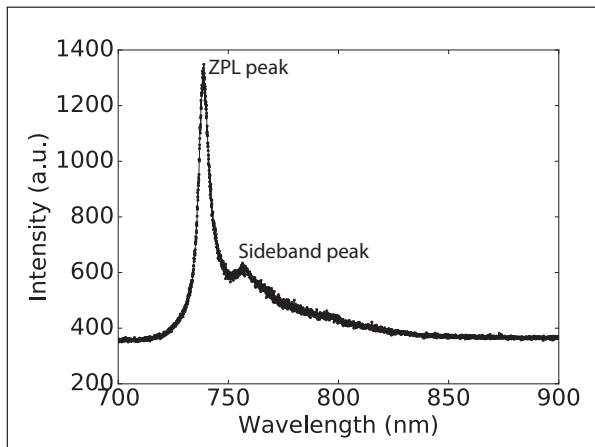


Figure 6.6: Representative spectrum of an emitter of group V exhibiting a sideband peak.

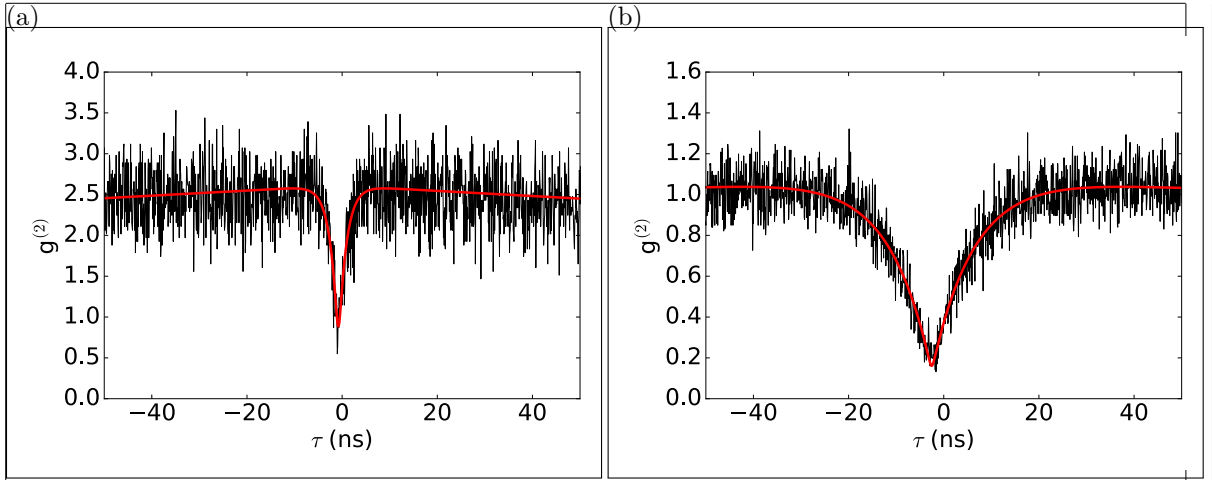


Figure 6.7: (a) Intensity autocorrelation function of emitter H1 at an excitation power of 15 pW. (b) Intensity autocorrelation function of emitter V1 at an excitation power of 200 pW, which is 25% of the saturation count rate.

equivocally distinguish between peaks stemming from a phonon sideband and peaks stemming from shifted, less intense SiV center ZPLs. The possibility exists, that some peaks identified as phonon sidebands are actually ZPLs stemming from shifted SiV centers. Therefore, we will focus our investigations on the more prominent sideband of group V.

Most of the spectra in group V exhibit a characteristic shape, composed of the ZPL and one strong sideband peak which is mostly shifted 37 meV to 43 meV. In reference [26] the 42 meV sideband peak is attributed to a non-localized (lattice) mode. It is also stated, that the local vibrational mode at 64 meV is much stronger than the 42 meV sideband peak. While the peak attributed to the non-localized mode is very strong in our measurements, we cannot identify the peak attributed to the local vibrational SiV center mode in the spectra of group V. A possible explanation is, that the lattice mode at 37 meV to 43 meV is so strong that the local vibrational mode at 64 meV cannot be separated from the tail of the lattice mode. In Figure 6.5 the distance between the center wavelength of the sideband peak and the center wavelength of the ZPL is plotted against the ZPL center wavelength. The distribution is fitted with a linear regression. We attribute the variance in the sideband shift to strain:

Adam Galis Erkenntnisse

## 6.1 Photon correlation measurements

The investigated SiV centers exhibit count rates of a few thousand to a few 100 000 cps. We carried out measurements of the photon statistics and found that about 3% of the SiV centers are single color centers. These measurements show, that the probability of finding a single emitter does not correlate in any way with the center wavelength of the ZPL or the linewidth of the ZPL. We found several single SiV centers with an antibunching dip down to about 0.2 and attribute the residual  $g^{(2)}(0)$  value to background fluorescence from the diamond host. For the utilized nanodiamonds an of the background measurement independent of SiV center photoluminescence is impossible, because the laser spot size is bigger than the nanodiamond.

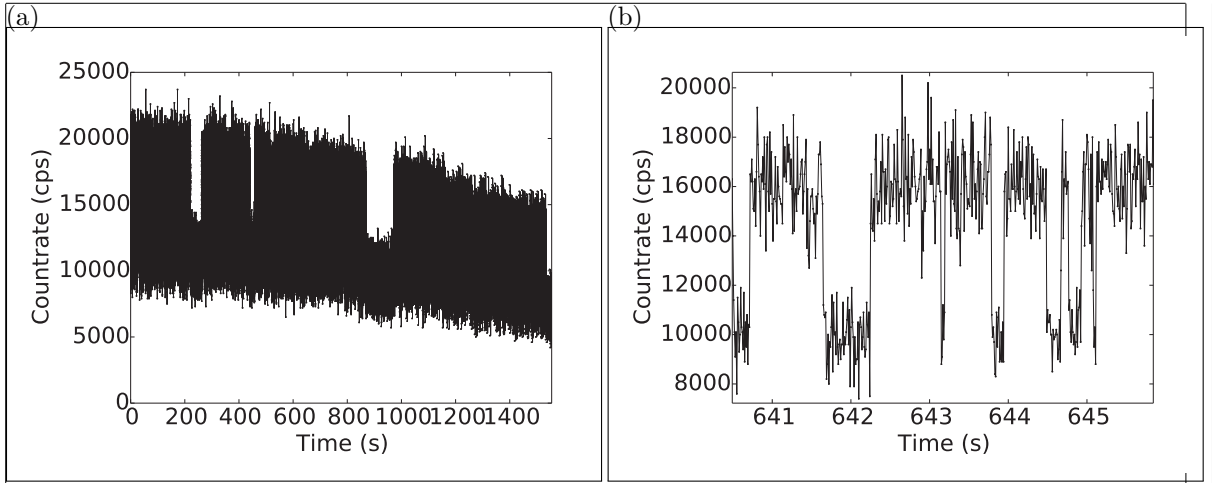


Figure 6.8: Distribution of countrate of a blinking level vs. its retention time in this level. (a) Time trace of the single emitter exhibiting the highest blinking rate. The variation of the countrate in the upper state is attributed to a drift of the setup. (b) Detail of the time trace of the same emitter.

Therefore, the SiV center will always be excited when the nanodiamond is illuminated. The measured lifetimes of the single SiV centers are in the range of 1 ns to 7 ns. Figure 6.7 shows the  $g^{(2)}$  functions of the two emitters introduced in subsection 6.0.1, emitter H1 and emitter V1.

Figure 6.7a shows the photon correlation function of emitter H1 at a power of 15  $\mu$ W. The fit of the data for an excitation power of 15  $\mu$ W yields a lifetime of the excited state of  $(1.6 \pm 0.1)$  ns. The  $g^{(2)}(0)$  values of the same fit is 0.88, which corresponds to eight equally bright emitters. However, the  $g^{(2)}(0)$  value is probably overestimated due to the fast dynamics of the emitter which cannot be fully resolved. Measurements of other SiV centers in group H yield  $g^{(2)}(0)$  values down to 0.2.

Figure 6.7b shows the  $g^{(2)}$  function of emitter V1 at an excitation power of 200  $\mu$ W, which is 25% of the saturation power of that emitter, which amounts to 1 mW. The  $g^{(2)}(0)$  values for yields  $0.16 \pm 0.06$ , therefore being a representative  $g^{(2)}$  measurement of single SiV centers. The fits yield a lifetime of the excited state of  $(6.3 \pm 0.2)$  ns. While it is not 0, it is well below 0.5, indicating single photon emission. The non-vanishing  $g^{(2)}(0)$  value is caused by background fluorescence of the diamond.

Several spectra contain multiple narrow distinct peaks at different ZPL center wavelengths. This circumstance is attributed to a nanodiamond containing more than one SiV center, each of which is subject to a different center wavelength shift. We choose narrow bandpass filters to perform independent measurements of each individual SiV center peak of such a spectrum. Therefore it is possible to measure  $g^{(2)}(0)$  values below 0.5 for each of those narrow peaks. Hence the individual peaks are identified as single emitters with a different ZPL center wavelength.

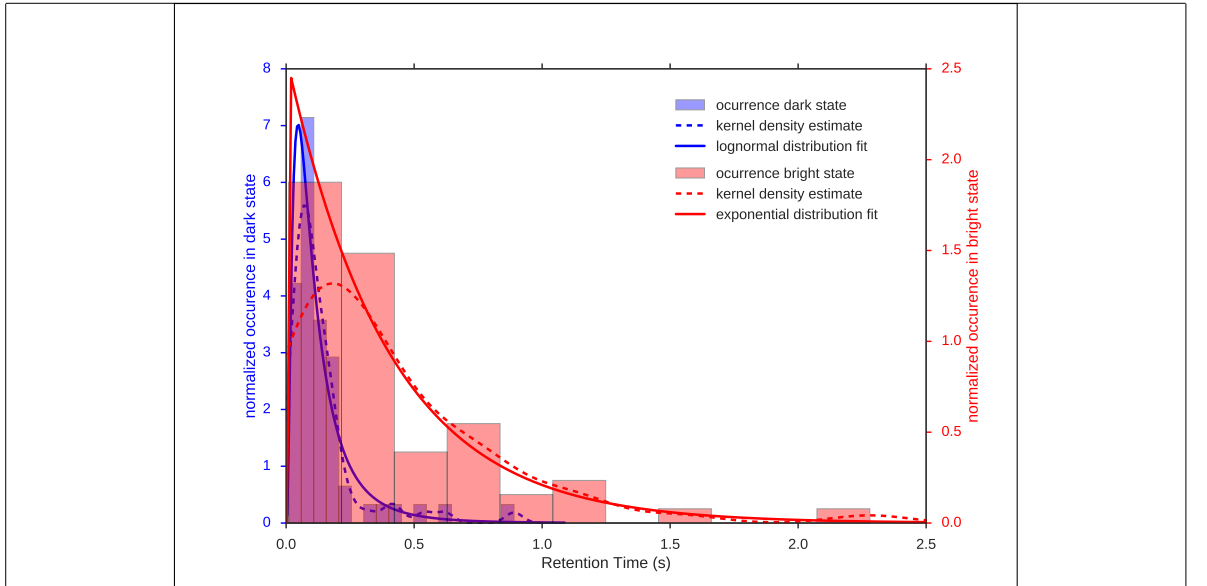


Figure 6.9: Retention times of the single emitter exhibiting the highest blinking rate in the bright (red) and dark (blue) states. The dashed line represents a kernel density estimation of the distribution of retention times. The y-axis is scaled to the normalized kernel density estimate. The red solid line is an exponential fit of the bright state retention times, the blue solid line is a lognormal fit of the dark state retention times. The fits are in good agreement with the data (p-values: red 0.92, blue 0.77)

### 6.1.1 Photostability

As mentioned in the previous section, the investigated SiV centers exhibit count rates of a few thousand to a few 100 000 cps. To further investigate the count rate, the luminescence time trajectory of the emitters which exhibit a dip at  $g^{(2)}(0)$  is evaluated. It is found that some of the observed emitters exhibit fluorescence intermittence, also called blinking (Figure 6.8). Blinking is attributed to temporal ionization of the color center during optical excitation, forming an optically inactive charge state [31, 17, 32]. Therefore the emitters change between states of higher and lower emission, i.e. brighter and darker states, called blinking levels. The time trace of the emitter is shown in Figure 6.8. In the overview picture (Figure 6.8a), a few blinking dips can be seen with retention times of up to a few minutes. The fact, that the count rate never drops to the dark count rate lets us assume, that there are at least two SiV centers present, one exhibiting fluorescence intermittence and one exhibiting a stable emission. When zooming in, shorter retention times are observable (Figure 6.8b). The retention times range from a few tens of milliseconds up to a few seconds with a few outliers exhibiting very long retention times up to a few hundred seconds.

The retention times of the bright and of the dark state exhibit different probability distribution functions and with that, different characteristic retention times. The red histogram in Figure 6.9 shows the retention times of the emitter in the bright state, whereas the blue histogram shows the retention times of the dark states (both omitting outliers with very long retention times). The dashed lines are kernel density estimators of the distribution of the respective retention times (i.e. every data point is represented with a Gaussian function and the resulting functions are added up to model the whole data). The red solid line is an expo-

ponential fit of the distribution of retention times in the bright state. The high p-value of 0.92 confirms the goodness of the fit. The mean and the median retention time in the bright state obtained by the exponential fit amount to  $(0.13 \pm 0.13)$  s and 0.09 s, respectively. While other literature about solid state quantum emitters reports an exponential probability distribution for both retention times in bright and dark states[33, 34], we found a lognormal probability distribution for the retention time in the dark state. The solid blue line in Figure 6.9 is a lognormal fit of the distribution of the retention times in the dark state. With a p-value of 0.77 it is by far the best model to describe the data distribution. For comparison: The p-value of an exponential fit only amounts to 0.36. The median retention time in the dark state obtained by the lognormal fit amounts to 0.10 s, therefore being a bit longer than the median retention time in the bright state (neglecting very long retention times which are treated as outliers).

We do not identify a correlation between the count rate of a blinking level and its retention time. However, there is a correlation between the position in the bimodal distribution and blinking: All but one emitters in group H exhibit blinking, where only one of the emitters in group V exhibits blinking (Figure 6.1). This dependency suggests that emitters in strained nanodiamonds are more likely to exhibit blinking.

We explain the observed blinking as a manifestation of the local crystal disorder due to dislocations and impurities which act as a trap for the excited electron and therefore switching the emitter to the dark state [33]. The assumption that dislocations and impurities are responsible for blinking emitters is in agreement with our findings in ??, where we attribute the Raman line at wavenumbers lower than the value of pristine diamond to damage of the diamond lattice.

---

---

## **Chapter 7**

## **discussion**

---

---

## **Chapter 8**

# **Conclusion**

In conclusion...

---

---

## **Appendix A**

### **Text of Minor Interest**

Some data

# Bibliography

- [1] J Y Cheung, C J Chunnillall, E R Woolliams, N P Fox, J R Mountford, J Wang, and P J Thomas. The quantum candela: a re-definition of the standard units for optical radiation. *Journal of Modern Optics*, 54(2-3):373–396, jan 2007. 1, 2
- [2] Current definitions of the SI units. 1
- [3] Joanne C Zwinkels, Erkki Ikonen, Nigel P Fox, Gerhard Ulm, and Maria Luisa Rastello. Photometry, radiometry and ‘the candela’: evolution in the classical and quantum world. *Metrologia*, 47(5):R15–R32, oct 2010. 2
- [4] Charles. Santori, David. Fattal, and Yoshihisa. Yamamoto. *Single-photon devices and applications*. Wiley-VCH, 2010. 5
- [5] Mark (Anthony Mark) Fox. *Quantum optics : an introduction*. Oxford University Press, 2006. 7
- [6] Richard D. Younger, K. Alex McIntosh, Joseph W. Chludzinski, Douglas C. Oakley, Leonard J. Mahoney, Joseph E. Funk, Joseph P. Donnelly, and S. Verghese. Crosstalk analysis of integrated Geiger-mode avalanche photodiode focal plane arrays. *Advanced Photon Counting Techniques III*, 7320:73200Q1–12, 2009. 8
- [7] R F Davis. *Diamond Films and Coatings: Development, Properties, and Applications*. Hébert, Alexandre-Martin-Stanislas. Noyes Pub., 1993. 9
- [8] K H O'Donovan. Synthetic diamond. 9
- [9] Valery a. Davydov, a. V. Rakhmanina, S. G. Lyapin, I. D. Il'ichev, K. N. Boldyrev, a. a. Shiryaev, and Viatcheslav N. Agafonov. Production of nano- and microdiamonds with Si-V and N-V luminescent centers at high pressures in systems based on mixtures of hydrocarbon and fluorocarbon compounds. *JETP Letters*, 99(10):585–589, 2014. 10
- [10] John W. Arblaster. Crystallographic Properties of Iridium. *Platinum Metals Review*, 54(2):93–102, 2010. 10
- [11] S. Gsell, M. Fischer, R. Brescia, M. Schreck, P. Huber, F. Bayer, B. Stritzker, and D. G. Schlom. Reduction of mosaic spread using iridium interlayers: A route to improved oxide heteroepitaxy on silicon. *Applied Physics Letters*, 91(6):061501, aug 2007. 10
- [12] Robert F. Davis, editor. *Diamond Films and Coatings*. Noyes Pub., 1993. 10
- [13] S. Gsell, T. Bauer, J. Goldfuß, M. Schreck, and B. Stritzker. A route to diamond wafers by epitaxial deposition on silicon via iridium/yttria-stabilized zirconia buffer layers. *Applied Physics Letters*, 84(22):4541, may 2004. 11

- [14] Matthias Schreck, Jes Asmussen, Shinichi Shikata, Jean-Charles Arnault, and Naoji Fujimori. Large-area high-quality single crystal diamond. *MRS Bulletin*, 39(06):504–510, jun 2014. 11
- [15] Oliver A. Williams and Milos Český Nesládek. Growth and properties of nanocrystalline diamond films. *Phys. status solidi*, 203(13):3375–3386, oct 2006. 13
- [16] Peter Zapol, Michael Sternberg, Larry Curtiss, Thomas Frauenheim, and Dieter Gruen. Tight-binding molecular-dynamics simulation of impurities in ultrananocrystalline diamond grain boundaries. *Physical Review B*, 65(4):045403, 2001. 14
- [17] Elke Neu, Mario Agio, and Christoph Becher. Photophysics of single silicon vacancy centers in diamond: implications for single photon emission. *Optics Express*, 20:19956–19971, jul 2012. 14, 17, 30
- [18] M. S. Dresselhaus and R. Kalish. *Ion Implantation in Diamond, Graphite and Related Materials*, volume 22 of *Springer Series in Materials Science*. Springer Berlin Heidelberg, Berlin, Heidelberg, 1992. 19
- [19] AM Zaitsev. *Optical properties of diamond: a data handbook*. 2001. 20
- [20] Steven Prawer and Robert J Nemanich. Raman spectroscopy of diamond and doped diamond. *Philosophical Transactions of the Royal Society A: Mathematical, Physical and Engineering Sciences*, 362(1824):2537–2565, nov 2004. 20, 21
- [21] J. O. Orwa, K. W. Nugent, D. N. Jamieson, and S. Prawer. Raman investigation of damage caused by deep ion implantation in diamond. *Physical Review B - Condensed Matter and Materials Physics*, 62(9):5461–5472, sep 2000. 20
- [22] Andrea Carlo Ferrari and John Robertson. Raman spectroscopy of amorphous, nanosstructured, diamond-like carbon, and nanodiamond. *Philosophical Transactions of the Royal Society of London A: Mathematical, Physical and Engineering Sciences*, 362(1824):2477–2512, 2004. 20
- [23] Carsten Arend, Jonas Nils Becker, Hadwig Sternschulte, Doris Steinmüller-Nethl, and Christoph Becher. Photoluminescence excitation and spectral hole burning spectroscopy of silicon vacancy centers in diamond. *Physical Review B*, 94(4):045203, jul 2016. iv, 23, 25
- [24] Julia Benedikter, Hanno Kaupp, Thomas Hücker, Yuejiang Liang, Alexander Bommer, Christoph Becher, Anke Krueger, Jason M. Smith, Theodor W. Hänsch, and David Hunger. Cavity-Enhanced Single-Photon Source Based on the Silicon-Vacancy Center in Diamond. *Physical Review Applied*, 7(2):024031, 2017. iv, 24, 25
- [25] Elke Katja Neu. *Silicon vacancy color centers in chemical vapor deposition diamond : new insights into promising solid state single photon sources*. PhD thesis, 2012. iv, 24, 25
- [26] Andreas Dietrich, Kay D Jahnke, Jan M Binder, Tokuyuki Teraji, Junichi Isoya, Lachlan J Rogers, and Fedor Jelezko. Isotopically varying spectral features of silicon-vacancy in diamond. *New J. Phys.*, 16(11):113019, nov 2014. 25, 28
- [27] Elke Neu, David Steinmetz, Janine Riedrich-Möller, Stefan Gsell, Martin Fischer, Matthias Schreck, and Christoph Becher. Single photon emission from silicon-vacancy

- colour centres in chemical vapour deposition nano-diamonds on iridium. *New Journal of Physics*, 13(2):25012, feb 2011. 25, 26
- [28] E. Neu, Carsten Arend, E. Gross, F. Guldner, C. Hepp, D. Steinmetz, E. Zscherpel, S. Ghodbane, H. Sternschulte, D. Steinmüller-Nethl, Y. Liang, A. Krueger, Christoph Becher, Et Al., Et al., Et Al., and Et Al. Narrowband fluorescent nanodiamonds produced from chemical vapor deposition films. *Appl. Phys. Lett.*, 98(24):243107, jun 2011. 25
- [29] GergÅŠ Thiering and Adam Gali. Complexes of silicon, vacancy, and hydrogen in diamond: A density functional study. *Physical Review B*, 92(16):165203, oct 2015. 26
- [30] Elke Neu, Martin Fischer, Stefan Gsell, Matthias Schreck, and Christoph Becher. Fluorescence and polarization spectroscopy of single silicon vacancy centers in heteroepitaxial nanodiamonds on iridium. *Phys. Rev. B*, 84(20):205211, nov 2011. 26
- [31] Uwe Jantzen, Andrea B Kurz, Daniel S Rudnicki, Clemens Schäfermeier, Kay D Jahnke, Ulrik L Andersen, Valery A Davydov, Viatcheslav N Agafonov, Alexander Kubanek, Lachlan J Rogers, and Fedor Jelezko. Nanodiamonds carrying silicon-vacancy quantum emitters with almost lifetime-limited linewidths. *New Journal of Physics*, 18(7):073036, jul 2016. 30
- [32] Adam Gali and Jeronimo R. Maze. Ab initio study of the split silicon-vacancy defect in diamond: Electronic structure and related properties. *Physical Review B*, 88(23):235205, dec 2013. 30
- [33] C Bradac, T Gaebel, N Naidoo, M J Sellars, J Twamley, L J Brown, A S Barnard, T Plakhotnik, A V Zvyagin, and J R Rabeau. Observation and control of blinking nitrogen-vacancy centres in discrete nanodiamonds. *Nature nanotechnology*, 5(5):345–9, may 2010. 31
- [34] Amanuel M. Berhane, Carlo Bradac, and Igor Aharonovich. Photoinduced blinking in a solid-state quantum system. *Physical Review B*, 96(4):041203, jul 2017. 31

---

---

# Index

$g^{(2)}$  function, 7

Hanbury Brown and Twiss, 4

Hanbury Brown and Twiss setup, 7

LHC, 3

photon autocorrelation function, 7